GEORG-AUGUST-UNIVERSITÄT
GÖTTINGEN

Fakultät für
Physik

Bachelor's Thesis

Dynamik in einem wasser-fluidisierten Bett

Dynamics in a water fluidized bed

prepared by

Sara Lea Gadeberg

from Westerstede

at the Max Planck Institute for Dynamics and Self-Organization,
Department: Dynamics of Complex Fluids

Thesis Period: 12th November 2012 until 18th February 2013

First Referee: Dr. Matthias Schröter

Second Referee: Prof. Dr. Sarah Köster

Abstract

In this thesis, the particle dynamics in liquid fluidized beds are analyzed. In order to do this x-ray images (radiographs) are taken in water fluidized beds of glass and ceramic beads (diameter $d \approx 200$ µm). When taking the radiographs as a function of time macroscopic and microscopic motion can be investigated.
The collective bead movement (macroscopic motion) manifests in density fluctuations within the bed. The analysis of the change in the gray-scale values allows us to see whether density fluctuations can be measured with the experimental setup that was used.
The microscopic particle dynamics are studied tracking single glass beads of the fluidized bed and analyzing their trajectories. The computed mean squared displacement indicates the particle motion on the microscopic scale.
For the different experimental setups convection is observed inhibiting particle movement on the microscopic scale without an overlaying macroscopically imposed motion.

Keywords: Driven Suspension, Granular Matter, Water Fluidized Bed, Particle Tracking, Diffusion

Zusammenfassung

In dieser Arbeit wird die Dynamik in flüssig-fluidisierten Betten untersucht. Hierzu werden Röntgenbilder von wasser-fluidisierten Betten aus Glas- bzw. Keramikkugeln (Durchmesser $d \approx 200$ µm) aufgenommen. Durch Aufnahme einer Zeitreihe von Röntgenbildern können so makroskopische sowie mikroskopische Bewegungen verfolgt werden.
Die makroskopischen Bewegungen können als Dichteschwankungen innerhalb des Bettes wahrgenommen werden. Die Tauglichkeit des verwendeten Versuchsaufbaus für die Untersuchung von Dichteschwankungen kann durch eine Untersuchung der Änderung der Grauwerte über die Zeit festgestellt werden.
Mikroskopische Bewegungen werden über das Verfolgen einzelner Glaskugeln untersucht. Werden die Trajektorien der Kugeln bezüglich der mittleren quadratischen Verschiebung ausgewertet, so kann eine Aussage über die Art ihrer mikroskopischen Bewegung gemacht werden.
Aufgrund einer sich durch alle Versuchsreihen ziehenden Konvektionsrolle konnten lediglich Teilchenbewegungen analysiert werden, die von einer zugrundeliegenden makrokopischen Bewegung beeinflusst waren.

Stichwörter: Angetriebene Suspensionen, Granulare Materie, Wasser-fluidisiertes Bett, Particle Tracking, Diffusion

Contents

1. Introduction

If you look up from this thesis and examine the room, you will see and at the same time not see one of the most interesting materials today's physicists are studying: Glass. Even though humans have been using glass in their everyday life for centuries, many open questions concerning the physical properties of this material still remain unanswered.

Contradictory to what we refer to as a glass in our everyday life, the physical definition of glass includes any solid that does not show an organized molecular pattern (crystal pattern), which includes some plastics or ceramics composed of randomly distributed molecules. A glass can be formed when a liquid is supercooled – meaning rapidly cooled below its melting temperature – if no crystalization process sets in. Unlike a liquid congealing into a crystalline solid, the glass transition does not have latent heat. The molecules move slower and slower until they seem to stop moving at all; no real phase transition occurs: *a glass remains liquid.*

During the glass-transition the size and lifetime of mobile and immobile regions increases. This effect is referred to as dynamical heterogeneity and yields the side effect that single grains can get trapped by other grains forming a cage around them for an intermediate time, from which – when looking at longer periods of time – they can escape yet to be trapped again.
In general the glass transition is characterized by stagnation of macroscopic motion, while microscopic motion persists. The dynamics of a liquid in the glass state are slowed down extensively in comparison to those observed at higher temperatures, additionally the viscosity and diffusity of a glass are strongly temperature dependent, while the structure of the glass remains unchanged, i.e. remains liquid-like.

Glass-forming liquids usually consist of relatively open structures, which are observed for granular materials as well. It seems deductive to look for glass transition

phenomena in granular systems. One specific model system being the fluidized bed, for which characteristics of the glass transition have already been observed [1]. The theoretical simplicity of fluidized beds would make them ideal candidates to study glass transitions.

Before glass-like behavior can be studied, some general questions on the dynamics of a fluidized bed need to be answered. In this thesis, the particle dynamics in water-fluidized beds of glass and cermaic beads are studied. On the macroscopic scale, density fluctuations in a water-fluidized bed are studied to determine homogenous and non-homogeneous movement. On the microscopic scale, single glass beads are tracked to see if they perform a random walk, i.e. showing diffusive behavior. The dynamics are studied with an x-ray unit taking radiographs of the bed.

The thesis is organized as follows: Chapter 2 provides the required theoretical background of microscopic motion in colloids, of granular materials and of fluidized beds. Chapter 3 presents the experimental setup and the tracer particles used. Chapter 4 explains the methods used to analyze the macroscopic motion in the examined fluidized beds and shows some results. Chapter 5 starts with an introduction to the algorithms used for image processing followed by the analysis of microscopic motion. Chapter 6 summarizes the conclusions drawn from the previous chapters and gives some ideas for modifications on the experimental setup.

2. Theory

This chapter gives a short summary of the theoretical background, that is needed to follow the experiments and analysis performed later. First, a short characterization of microscopic dynamics observed for colloids is given to introduce some general terms used when describing particle movement. Second, some basic knowledge of granular material is presented. Third, fluidized beds and their macroscopic and microscopic dynamics are introduced.

2.1. Microscopic dynamics of colloids

Colloids are microscopic particles (diameter: 1 nm – 1 µm) distributed in another material, e.g. a liquid. In general their dynamics are influenced by thermal energy. It might be interesting to see if some microscopic dynamics observed for colloids can be applied to the granular materials introduced later, especially the fluidized bed. This section introduces some general terms and observations on microscopic dynamics of colloids, which should afterwards be compared to fluidized beds.

2.1.1. Brownian motion

Colloids distributed in a liquid show a temperature-dependent mean velocity, changing their direction of movement when colliding with other molecules. This results in a random movement at the microcopic scale, even if the liquid is motionless on the macroscopic scale. This is known as BROWNian motion. The velocity distribution of BROWNian motion has the shape of a MAXWELL-BOLTZMANN distribution [2] (see figure 1); without underlaying macroscopic gradients the velocity distribution is isotropic (i.e. the same in all spacial directions).

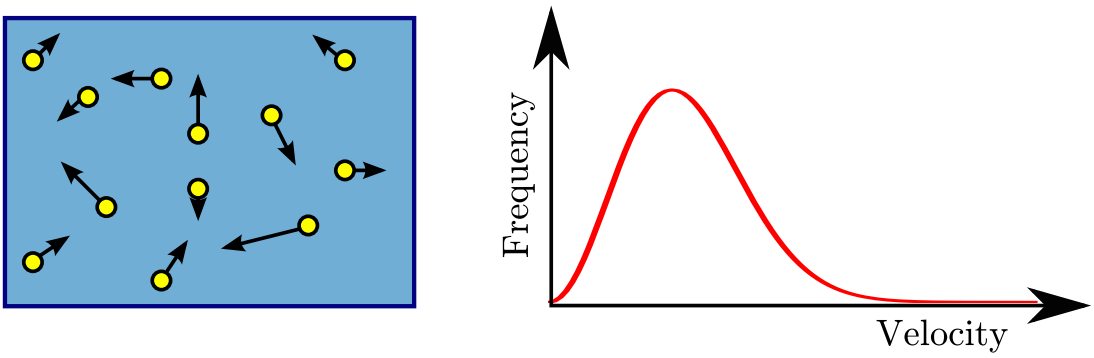

Figure 1: BROWNian motion of particles in a liquid (left) and their velocity distribution (right). Figure modified from [3].

2.1.2. Diffusion

As a side effect of the BROWNian motion, all particles in a liquid diffuse until no gradients (e.g. pressure or density) are left. Once no macroscopic gradient exists only self-diffusion of the particles is observed following FICK's second law:

$$\frac{\partial c(x,t)}{\partial t} = D_x \frac{\partial^2 c(x,t)}{\partial x^2} \qquad \text{(one-dimensional)},$$

where $c(x,t)$ is the concentration of the particles (in e.g. water) and D_x the self-diffusion constant in x-direction. For BROWNian motion this yields the EINSTEIN-SMOLUCHOWSKI-equation [4]

$$\langle [\Delta x(t)]^2 \rangle = 2D_x t, \tag{1}$$

where $\langle [\Delta x(t)]^2 \rangle$ is the mean squared step length with $\Delta x(t) = x(t+t_0) - x(t_0)$ representing the particle's displacement and t_0 is an arbitrary reference time.

2.1.3. Mean squared displacement

The mean squared displacement (MSD) is a measure for the mean distance a particle moves in a time interval τ. In general the MSD is calculated as an ensemble MSD, but for ergodic systems the MSD can be calculated as a time-average as well. A fractal self-diffusive system is ergodic [5], therefore the ensemble and time-average MSD are consistent. Figure 2 shows the MSD of different diffusion modes.

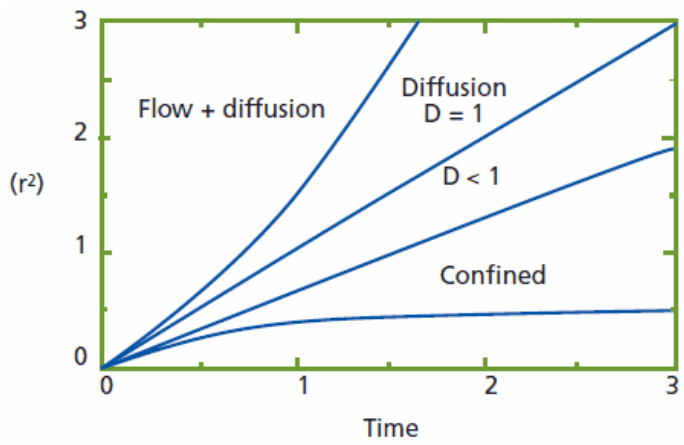

Figure 2: MSD (r^2) of different diffusion modes:
Freely diffusing particles follow the EINSTEIN-SMOLUCHOWSKI-equation (MSD $\propto \tau^{D=1}$). Particles whose diffusion is hindered or restricted to an area (confined) show a MSD $\propto \tau^{D<1}$. Particles transported by a flow show a MSD $\propto \tau^{D>1}$. Figure taken from [7].

Ensemble MSD

The ensemble MSD $\langle \Delta R^2(\tau) \rangle$ is calculated by analyzing the behavior of N equally prepared particles with trajectories $R_l(\tau)$ (an ensemble), where $R_l(0)$ is the initial position of the particle. For this approach the particle trajectories can be short compared to the amount N of particles analyzed.
The MSD of the particles for the time interval τ is calculated summing over the squared traveled distances $[R_l(\tau) - R_l(0)]^2$ of all particles:

$$\langle \Delta R^2(\tau) \rangle = \lim_{N\to\infty} \frac{1}{N} \sum_{l=1}^{N} [R_l(\tau) - R_l(0)]^2 \,. \tag{2}$$

Time-averaged MSD

The time-averaged MSD $\langle \Delta x^2(\tau) \rangle$ is calculated by analyzing the behavior of one long particle trajectory x of length M [6]. The trajectory is cut in different time intervals τ and the MSD is then calculated as the sum over the squared traveled distances in these intervals:

$$\langle \Delta x^2(\tau) \rangle = \frac{1}{M-\tau} \sum_{j=1}^{M-\tau} [x(j+\tau) - x(j)]^2 \,. \tag{3}$$

2.2. Granular materials

Assemblies of macroscopic solid particles that are not influenced by thermal energy (which means they are not influenced by BROWNian motion) are limited to grain sizes greater than 1 µm [8]. These assemblies are noncolloidal and referred to as granular materials. In general they are classified by shape and size of the grains. Granules consisting of spherically shaped grains are divided into two goups: polydisperse granular materials, which consist of differently sized spheres, and monodisperse granular materials, which consist of same sized spheres. Different states of matter have been observed in granular materials: While the grains are solid, the granular materials show solid, fluid-like or gas-like characteristics.
There are many effects to study when looking at granular materials, for example vertically shaken polydisperse granules show segregation due to granular convection, where large particles end up at top. Other effects are the density-dependence of expansion and compression of a granular material under shear stress [9] and the phenomenon of a glass-like transition [1] as previously mentioned.

2.2.1. Volume fraction

To characterize granular material the volume fraction ϕ is introduced. It gives a measure of the particle density by comparing the volume of the grains V_{solid} to the total volume V_{total} they occupy:

$$\phi := \frac{V_{\text{solid}}}{V_{\text{total}}}.$$

This volume (or packing) fraction depends on shape, surface and size distribution of the grains. Generally granular media packs looser for rough grain surfaces due to increased friction, whereas smooth particles are expected to pack denser [10, 11].

2.2.2. Granular suspension

A mixture of a noncolloidal solid granular material and a viscous fluid is called granular suspension. If the granular suspension comes to rest, sedimentation can

be observed resulting in two phases: the fluid and the sediment. In the sedimentation of a suspension the grains settle slower than one single grain in a fluid, due to the particle-particle interactions, this effect is known as hindered settling and results in a sharp line between suspension and fluid. For the volume fraction of the sediment of a granular suspension, it was shown that low settling velocities (e.g. using light particles or highly viscous fluids) result in less dense packings, because the grains transfer less kinetic energy when impinging on the already build sediment and therefore produce less shifting [10]. For polydisperse granular materials the sediment undergoes segregation, due to the different sedimentation velocities of differently sized grains [12].

A driven suspension is defined as a granular suspension never coming to rest, i.e. no sediment is formed. This could also be described as a continuous sedimentation. When a system becomes a driven suspension it undergoes a phase transition to a fluid-like state called fluidization. This effect is observed in fluidized beds, where a fluid flow is sent through granular material counteracting gravity.

2.3. Fluidized bed

Fluidized beds are used for many different applications, for instance in raw oil processing or chemical reactors. In general, a fluidized bed consists of a flow-through vessel, which is filled with a fluid (gas or liquid) and a granular material, placed on a fluid distributor (a schematic construction is shown in figure 3). Using a pump one can create a constant fluid flow from bottom to top; the flow is distributed homogeneously by the fluid distributor. The grains of the granule move based on buoyancy, gravity and drag imposed by constant upward flow.

A very important feature to have in mind when working with fluidized beds is the aging of particles, which occurs due to the fact that collisions smoothen their surfaces. In case the fluid is a liquid it can undergo aging effects due to bacteria or algea growth, which affects the liquid's density and viscosity. In a liquid fluidized bed the particle's surface might also be altered because of the deposition of biological material[1].

[1] Aging effects in a liquid fluidized bed were observed and presented in the master's thesis of W. Pätzold [13], who developed the experimental setup used in this thesis.

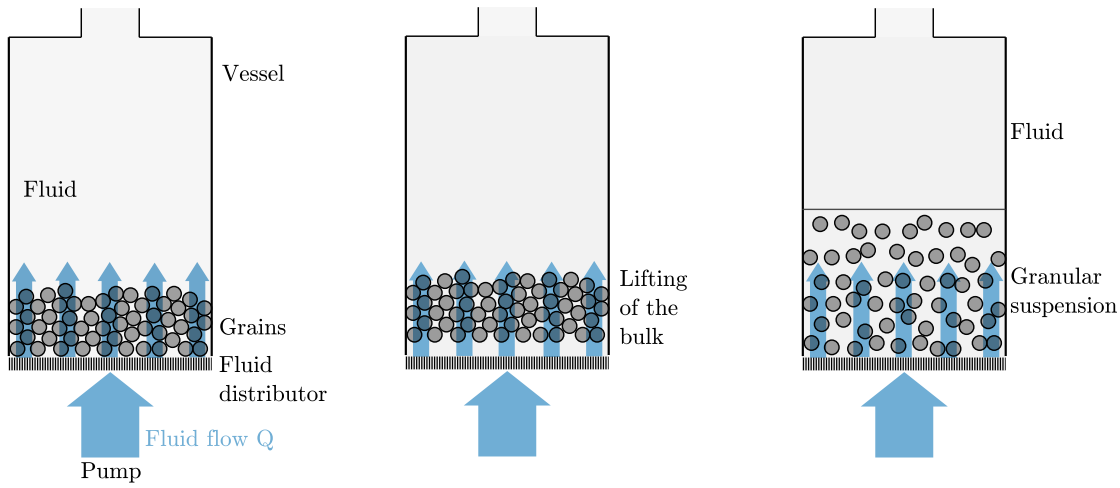

(3.1) Fixed bed for $Q < Q_{\text{crit}}$.

(3.2) Onset of fluidization for $Q = Q_{\text{crit}}$.

(3.3) Stationary fluidization state for $Q > Q_{\text{crit}}$.

Figure 3: Schematic construction of a fluidization cell.

2.3.1. Macroscopic dynamics in a fluidized bed

The macroscopic dynamics in a fluidized bed are divided into two fields: The macroscopic dynamics of the whole fluidized bed (reaction of the fluidized bed to different fluidization velocities resulting in different fluidization states) and the macroscopic dynamics in the fluidized bed (the density fluctuations in the stationary fluidization state).

Reaction to different fluidization velocities

Applying a fluid flow to a fluidized bed, the drag produces a pressure drop between bottom and top of the bed, which is increasing with the flow rate. For very small flow rates the particles remain at rest because this pressure drop is too small, a state known as the fixed bed (cf. figure 3.1). Increasing the flow rate, an onset of fluidization can be observed at the minimal flow rate, also known as the critical flow rate Q_{crit}, where all forces are balanced. This is observed as a lifting of the bulk of grains (cf. figure 3.2).
After fluidization sets in, the pressure drop will remain constant while the bed expands up to the stationary fluidization state, where the height of the suspension remains constant forming a sharp line between suspension and fluid (cf. figure 3.3).

In the stationary state the volume fraction of the granular material depends only on the applied fluid flow and the settling velocity a single grain would have. This is described by the RICHARDSON and ZAKI law, cf. [14].
Looking at fluid flows $Q >> Q_{\text{crit}}$ the grains get ejected through the top opening of the fluidization cell.
If the fluid flow is turned off, the remaining grains sediment on the distributor. The volume fraction of the sediment has been studied and it was shown that for a set of particles the volume fraction of the sediment only depends on the previous flowrate [15].

Density fluctuations

The dynamics of a fluidized bed in the stationary fluidization state can show a homogeneous or non-homogeneous behavior. A non-homogeneous bed is characterized by instabilities which manifest as e.g. *bubbles* (particle free parts of the suspension) traveling through the bed from bottom to top, *slugs* (alternation of high and low grain concentration) and *clusters* (regions of high grain concentration). Whether a fluidized bed is homogeneous or non-homogeneous depends on various factors [16]. In general, liquid fluidized beds (mainly particle-liquid-interactions) show more stable dynamics than gas fluidized beds (mainly particle-particle-interactions) [17].
Gas-fluidized beds have been classified by GELDART [18] by their grain size, density and behavior. GELDART postulated four groups (cf. figure 4) showing different dynamics:

- **Group A** "*aeratable*": Small grains with low densities show homogeneous dynamics for low fluidization velocities;
- **Group B** "*sandlike*": Intermediate grains with intermediate density show a small expansion and bubbles;
- **Group C** "*cohesive*": For very small or charged grains a homogeneous fluidization is nearly impossible;
- **Group D** "*spoutable*": Very big or very dense particles (or both) only fluidize for high energies and develop big bubbles.

For liquid fluidized beds no such characterization has been done, but first results suggest the groups to be different [13].

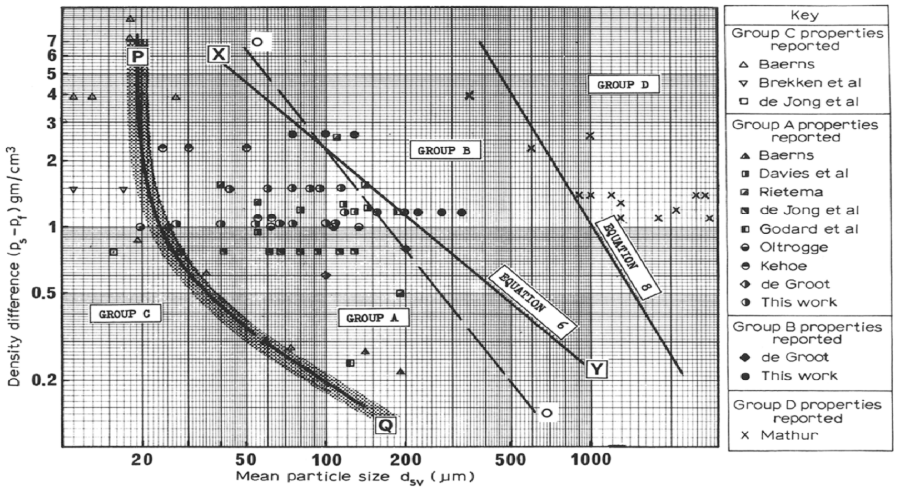

Figure 4: GELDART-diagram: Showing the density difference between grains and liquid as a function of the mean particle diameter. Figure taken from [18].

2.3.2. Microscopic dynamics in a fluidized bed

The characteristics of microscopic dynamics in a fluidized bed are still not completely experimentally analyzed. In theory, a homogeneously fluidized bed should show BROWNian motion and therefore self-diffusion [19]. This property can be investigated experimentally by checking whether particles in a fluidized bed perform a random walk, which is done by analyzing the MSD (cf. section 2.1.2 and 2.1.3).
When studying phase transitions and glass-like behavior of granular material, the kinetic granular temperature [20] is defined by the speed fluctuations of the fluidized particles. Glass-like behavior of fluidized beds has been observed when lowering the flow rate towards the minimal fluidization velocity, resembling a cooling of the system [1].

3. Experiments

In this chapter at first the general experimental setup including the construction of the fluidization cell and the x-ray unit used are described. Second, the use of different tracer particles is discussed. Third, the different compositions of the fluidized beds, for the analysis of density fluctuations and particle tracking, are described.

3.1. Experimental setup

The experimental setup (shown in figure 5) is arranged in a computed tomography scanner (the `nanotom`, see section 3.1.2).

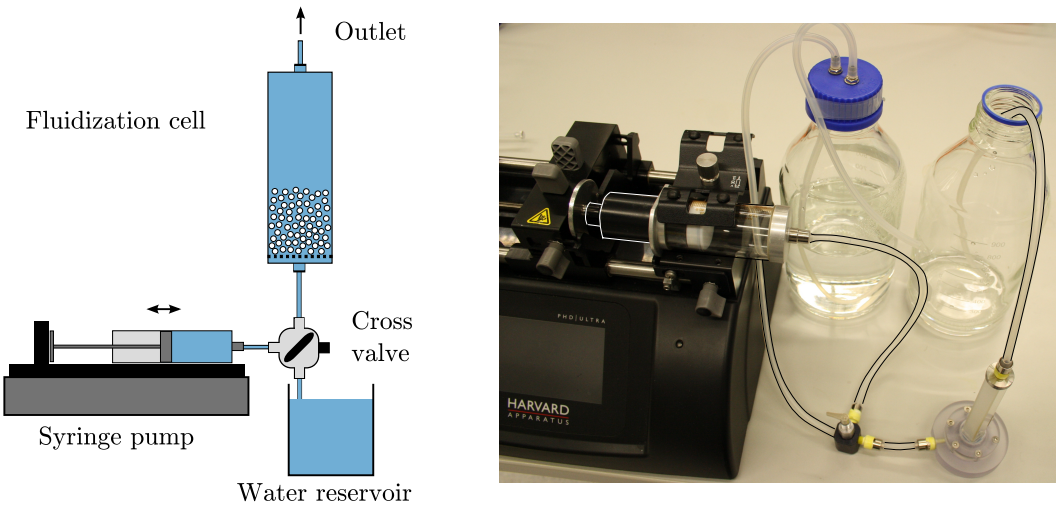

Figure 5: Experimental setup. Schematic figure modified from [13].

A cross valve connects a syringe pump (*Hamilton Gastight 1050* syringe and *Harvard PHD Ultra* pump) to a fluidization cell (more details in section 3.1.1) and to a water reservoir using silicone hoses (inner diameter: 2.0 mm, outer diameter: 4.8 mm).

The cross valve is utilized to switch manually between injecting water from the syringe pump into the fluidization cell and refilling the syringe pump from the water reservoir.

3.1.1. Fluidization cell

The fluidization cell[2] is built from a square tube cuvette (*Hellma Absorption Cell* no. 440-10-10) made from optical glass (crown glass). The empty cuvette has a transmittance of more than 80 % for wavelengths between 320 nm and 2500 nm, therefore the cuvette should only absorb little x-ray.
To create a flow-through cell the bottom of the cuvette is removed[3] resulting in a cuvette length of roughly 8 cm. The inner diameter of the cuvette is measured five times using a caliper, resulting in a mean value (with sample standard deviation) of (9.942 ± 0.006) mm and (9.66 ± 0.03) mm, where the second value gives the diameter perpendicular to the applied x-ray.
The cuvette is fixed on a base built from polycarbonate, absorbing only little x-ray, which is important when placing it in the `nanotom`. Through the base water can enter the cell passing a frit (*Vogelsberger Quarzglastechnik*, type Q4, pore size: $10 - 16$ µm) which provides a homogeneous flow.
The upper end of the cuvette is closed by a metal plug[4] with an opening of 2 mm to let water out. The plug can be unscrewed to fill particles into the cuvette.
The water used was cleaned with a *Milli-Q Integral Water Purification System* of the company *Millipore* and degasified with an ultrasonic bath.

3.1.2. X-ray unit: nanotom

The *Phoenix|x-ray* `nanotom` [21] (shown in figure 6.1) is equipped to take 3D x-ray micro computed tomographies, widely known as CT, and 2D radiographs of a sample. Objects can be studied based on their density, the atomic number of the components and the energy of the inflicted radiation. The `nanotom` has a resolution up to 0.2 µm (value given by the manufacturer).

---

[2] Designed and realized by W. Pätzold.
[3] Removed by the workshop for optics of the Max-Planck-Institute for Biophysical Chemistry.
[4] The plug was fitted by the workshop of fine mechanics of the MPI-DS.

(6.1) *Phoenix|x-ray* `nanotom` [21] and applied coordinate system.

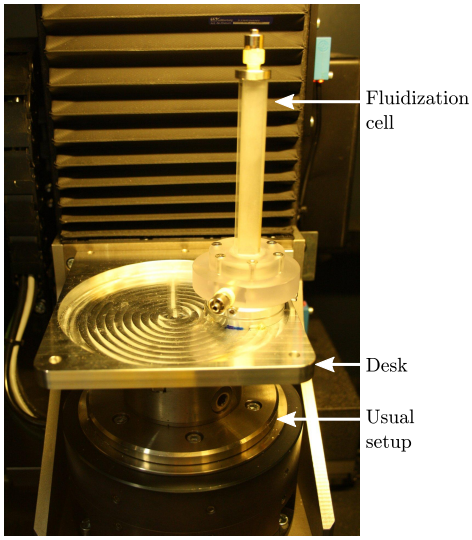

(6.2) Fluidization cell placed on a specifically designed desk.

Figure 6: X-ray unit: `nanotom`.

When the experimental setup described above is arranged in the `nanotom`, the fluidization cell is placed on a specifically designed desk[5] (see figure 6.2). The desk inhibits unwanted rotation of the `nanotom`-sample and collects leakage water in an indentation.
Some *parameters* of the `nanotom` can be varied by the user:

- The *detector position* (XD, ZD) and the *sample position* $(X = 0, Z, Y)$ determine the magnification of the radiographs. Because the fluidization cell is placed on a desk the values used are not accuarate and will therefore not be listed.

- The *binning* of the detector determines how many detector pixels are combined in horizontal and vertical direction to become a single pixel on the radiograph. In this thesis 4×4-binning is used which means that 1 pixel on the radigrams combines 16 pixels of the dectector.

- For a motionless setup the image sharpness increases, when increasing the *time* between taking the radiographs and the amount of radiographs to *average* over. When analyzing movement these parameters should have low values. In this

[5] The desk was designed by W. Keiderling and built by the workshop of fine mechanics of the MPI-DS.

thesis no averaged pictures are taken and the time between the pictures is 125 ms (lowest value available).

- In order to use a large range of the available gray-scale values the *voltage* U and the *current* I can be varied. In this thesis a voltage of $U = 160$ kV is used, the current is changed for the different experiments.

An example radiograph of the fluidization cell filled with beads and the applied coordinate system is shown in figure 7.

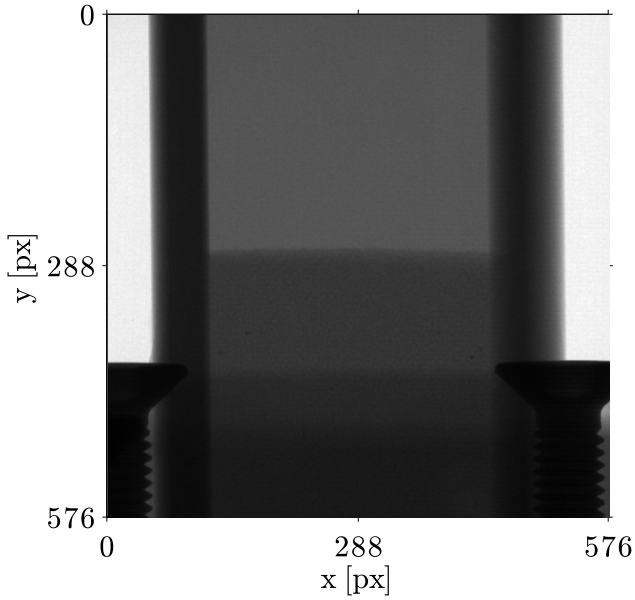

Figure 7: Radiograph of the filled fluidization cell taken by the `nanotom` and the applied coordinate system.

3.2. Tracer particles

In order to detect a single particle as a black dot in a fluidized bed with the `nanotom`, this tracer particle needs to have a higher absorption of the x-ray compared to the non-tracer particles. Simply using a different material for the tracer particle results in different dynamics. Therefore, it is more convenient to coate some of the beads, that are used in the fluidized bed, with a thin layer of a material of higher atomic number and use them as tracer particles. The higher atomic number results in a larger atomic weight and a higher absorbtion of the x-ray.
It would be most convenient to use fully and evenly coated gold tracer particles with a coating layer of > 1 µm. As no such particles are available for this thesis, different gold- and silver-coated tracer particles are tested in the `nanotom`.

3.2.1. Silver tracers

Two different types of fully-coated silver tracers are available and tested in the `nanotom`:

1. The detection of fully coated silver *Cospheric* glass beads of diameter 86 – 110 µm in a bulk of *Whitehouse* (*WH*) glass beads of diameter 106 – 125 µm is not possible.

2. The detection of fully coated silver *WH* glass beads of diameter 180 – 212 µm in a bulk of *WH* glass beads of diameter 180 – 212 µm is possible but barely sufficient as the gray-scale value of the tracers hardly differed from that of the uncoated glass beads. The particles are coated two times in a wet chemical procedure described in appendix A with the help of A. M. Pries and J. Murison. In general the chemically coated tracer particles are coated unevenly and partly very thin (see figure 8.1).

3.2.2. Gold tracers

Three different types of gold tracers are tested in the `nanotom`:

1. The detection of fully-coated *CreaVac* glass beads of diameter 350 µm and a gold layer of 100 nm in a bulk of soda lime spheres of diameter 315 – 355 µm is not possible.

2. The detection of half-coated *WH* glass beads of diameter 250 – 300 µm with a gold layer of 450 nm in a bulk of 250 – 300 µm *WH* glass beads is not possible. The particles where coated with an evaporation machine at the University of Göttingen with the help of U. Vetter and H.-G. Gehrke.

3. The detection of half-coated (1 µm) *WH* glass beads of diameter 180 – 212 µm in a bulk of 180 – 212 µm *WH* glass beads is possible (see figure 8.2). The particles are sputter coated at the MPI-DS with the help of U. Krafft with a coating of 0.06 µm chromium and 1 µm gold.

In general the half-coated particles are barely sufficient for tracking because they are easily misdetected due to their self-rotation (changing size of the black area on the radiograph). Unfortunately the scope of this thesis did not allow to produce fully coated gold tracer particles with the sputter setup.

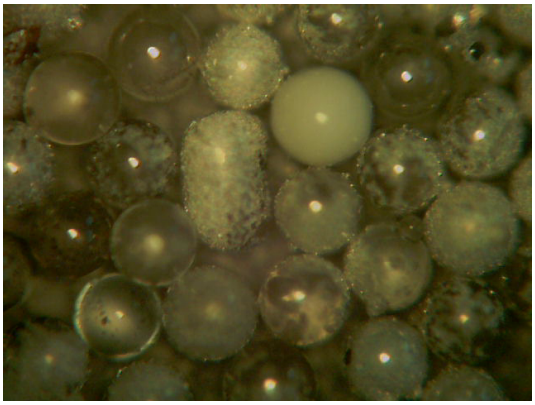

(8.1) Fully coated silver tracers under the microscope. The particles are coated unevenly and partly very thin.

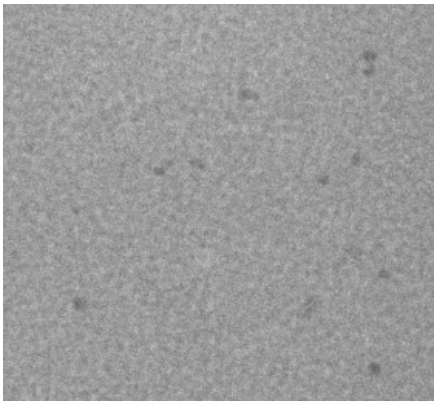

(8.2) Half-coated gold tracers in the `nanotom`. The size of the darker spots depends on the orientation of the particles.

Figure 8: Fully coated silver and half-coated gold tracers.

3.3. Composition of the studied fluidized beds

Setup 1: To study density fluctuations in a fluidized bed ceramic beads (*Sigmund Lindner GmbH*, type Z, 67.5 % ZrO_2 + HfO_2 and 27.5 % SiO_2 with 5 % other components) of diameter $300 - 315$ µm are used, because they are expected to show inhomogeneous dynamics. The beads are filled in the fluidization cell and fluidized with *Millipore*-water at different fluidization velocities ($v = 0;\ 30;\ 40;\ 60\ \frac{\text{ml}}{\text{min}}$). `Nanotom` parameter: $I = 120$ µA.

Setup 2: To compare the results from setup 1 to a supposedly homogeneous fluidization, *WH* glass beads of diameter $250 - 300$ µm are filled in the fluidization cell and fluidized with *Millipore*-water at different fluidization velocities ($v = 10;\ 15;\ 25\ \frac{\text{ml}}{\text{min}}$). `Nanotom` parameter: $I = 70$ µA.

Setup 3-5: To analyze the microscopic motion in a fluidized bed different amounts of *WH* glass beads of diameter $180 - 212$ µm and tracer particles (see section 3.2) are filled in the fluidization cell. The particles are fluidized with *Millipore*-water at different fluidization velocities (later referred to as different runs) for $1 - 3$ min. For best detection of the tracer particles a current of $I = 60$ µA is applied.

- **Setup 3:** $v = 0;\ 3;\ 4;\ 6\ \frac{\text{ml}}{\text{min}}$, fully coated silver tracers.
- **Setup 4:** $v = 0;\ 3;\ 4;\ 5;\ 6\ \frac{\text{ml}}{\text{min}}$, fully coated silver tracers and half-coated gold tracers.
- **Setup 5:** $v = 0;\ 3;\ 6\ \frac{\text{ml}}{\text{min}}$, half-coated gold tracers.

For all three setups no movement can be observed for fluidization velocities of $v < 3\ \frac{\text{ml}}{\text{min}}$. For fluidization velocities $v > 6\ \frac{\text{ml}}{\text{min}}$ the tracer particles are blurred too much for tracking and for fluidization velocities $v > 8\ \frac{\text{ml}}{\text{min}}$ the tracer particles cannot be detected anymore.

No further studies on the fluidized beds are performed because it is not possible to get rid of a convection cell that formed during operation. The convection cell might be originating in a small deformation of the fluidization cell; between bottom and top the cuvette shifts about 0.5 mm in x-direction. Trying to straighten the cell with a spirit level, when arranging it in the nanotom, only results in a shifting of the convection cell to the other side (probably because the distributor is not perpendicular to the cell anymore).

4. Analysis of macroscopic motion

In this chapter the data gained from setup 1 and 2 of the experiments described in the previous chapter are analyzed to see, if an analysis of density fluctuations within the fluidized bed is possible using the `nanotom`. This could help to postulate the GELDART groups (see section 2.3.1) for liquid fluidized beds.

4.1. Density fluctuations

In general an inhomogeneous fluidization (bubbels, slugs or clusters) is expected for setup 1, while a homogeneous fluidization is expected for setup 2. To analyze density fluctuations in the beds the change in the gray-scale value needs to be analyzed over time. Density fluctuations, e.g. traveling waves or bubbles, should appear as patterns like diagonal lines.
To analyze the change in the gray-scale values as a function of time the radiographs taken of setup 1 and 2 are loaded into `MATLAB` [22] and cut to the relevant image section, only including the fluidized bed without the rim of the fluidization cell. Next the average gray-scale values are calculated over 10 columns and 1 row (over an 1×10 px matrix). An example picture is shown in figure 9.

In the next step the averaged gray-scale values of each column are plotted over time. Figure 10 shows the change in the averaged gray-scale values in y-direction over time for different fluidization velocities. A column close to the center ($x = 201$ px) of the fluidized bed of setup 1 was analyzed. As expected the gray-scale values of the fixed bed in figure 10.1 only depend on the y-position and do not change over time. For fluidization velocities of $v = 40\ \frac{\text{ml}}{\text{min}}$ and $v = 60\ \frac{\text{ml}}{\text{min}}$ the gray-scale values seem to fluctuate over time, but no pattern can be seen in figures 10.2 and 10.3.

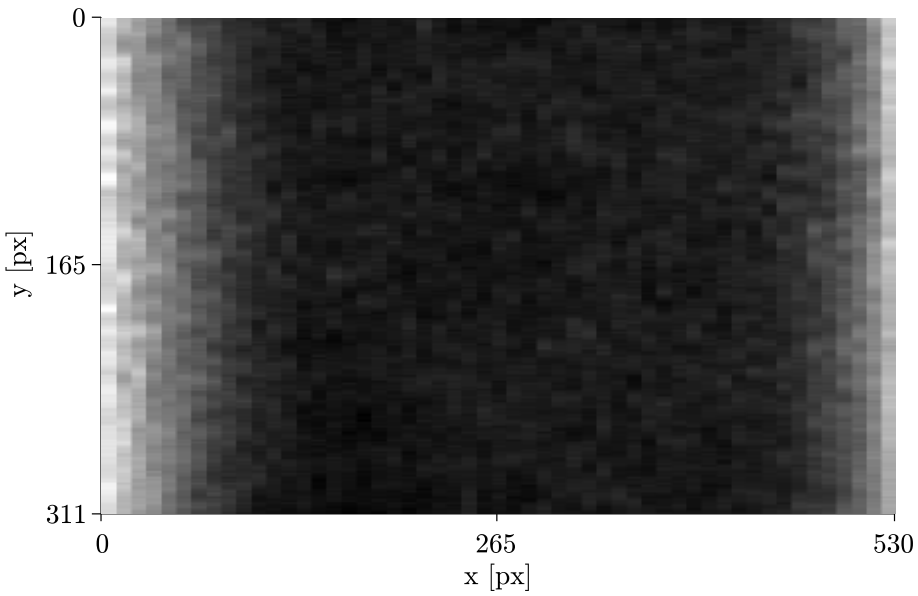

Figure 9: Averaged gray-scale values of a radiograph. Averaged over an 1×10 px matrix for a radiograph of setup 1 (ceramic beads; $300 - 315$ µm) at fluidization velocity $v = 60\ \frac{\text{ml}}{\text{min}}$.

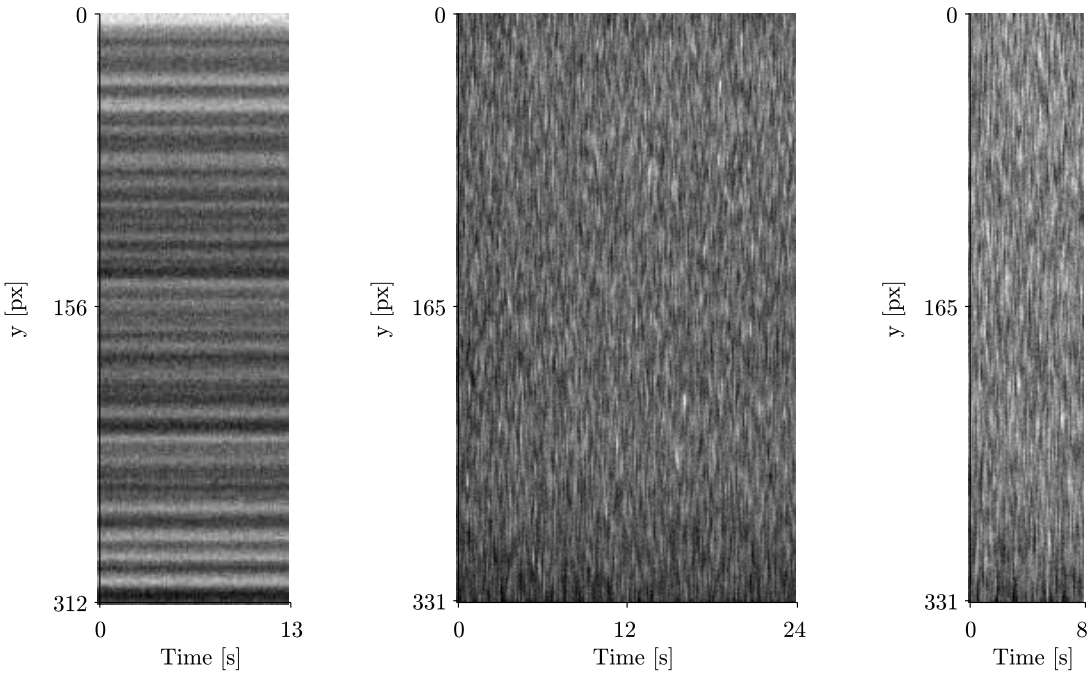

(10.1) $v = 0\ \frac{\text{ml}}{\text{min}}$. **(10.2)** $v = 40\ \frac{\text{ml}}{\text{min}}$. **(10.3)** $v = 60\ \frac{\text{ml}}{\text{min}}$.

Figure 10: Particle density in a non-homogeneously fluidized bed: Change in the gray-scale values at different y-positions over time at a constant x-position (201 px). Different fluidization velocities v. Radiographs from setup 1.

When comparing figure 10.2 and 10.3 to figure 11, where the change in the gray-scale value in y-direction as a function of time is shown for setup 2 (homogeneous fluidization), no significant difference can be identified, except for the generally darker ceramic beads (higher absorption).

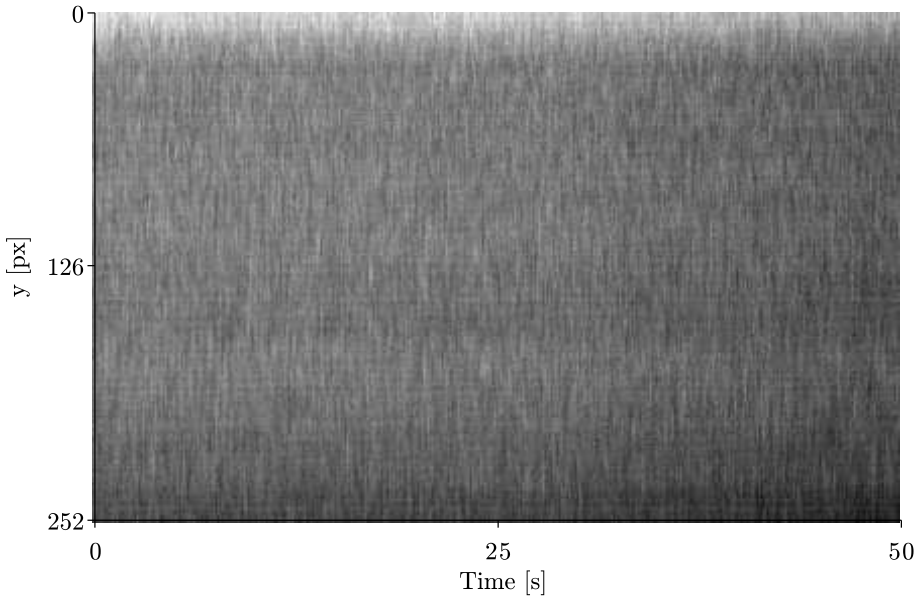

Figure 11: Particle density in a homogeneously fluidized bed: Change in the gray-scale values at different y-positions as a function of time at a constant x-position (201 px). Fluidization velocity of $v = 25\ \frac{\text{ml}}{\text{min}}$. Radiographs from setup 2 (glass beads $250 - 300$ µm).

For all other columns no patterns can be identified either. Therefore we conclude: An analysis of density fluctuations in setup 1 and 2 with the `nanotom` is not possible. This might be because the density fluctuations have a shorter timescale, than the time between taking the radiographs, or they are not strong enough to make a difference in absorption. Another reason could be the loss of information due to projection of a 3D process onto a 2D plane (i.e. averaging over multiple layers of bubbles). Maybe a convection cell manifested in setup 1 and 2 and no density fluctuations like slugs can manifest, due to this stronger overlaying movement. Whether there is a convection cell cannot be determined, because there are no tracer particles in the beds.

Ideas for modifications on the experimental setup, that might allow the observation of density fluctuations, are presented in Chapter 6.

5. Analysis of microscopic motion

In this chapter the data from setup 3 - 5 are analyzed to study the microscopic motion in the fluidized beds by particle tracking. First, the image processing of the radiographs is introduced, including the algorithm used to locate the particles on the pictures. Second, the routine of tracking the particles through a set of radiographs is desribed and a resolution/noise level of the x-ray unit is determined. Third, the reconstructed particle trajectories are discussed. Fourth, the particle velocity in the fluidized beds is analyzed and the trajectories are cut into representative segments. In the last part the mean squared displacement is calculated for a numerically simulated random walk and the particle trajectories from setup 3 - 5.

5.1. Image processing

In this section the routines implemented with `MATLAB`, which are used to analyze the radiographs taken with the `nanotom`, are described. `MATLAB` loads the radiographs as <576×576 uint16>-arrays, meaning that 16 bit integer values (from 0 to 65 535) can be assigned to the gray-scale values in an array of pixel size 576×576. The values recorded with the `nanotom` show a range far below 65 535. For analysis the coordinate system introduced in figure 7 is used: $x(j)$ is assigned to the columns with column indices $j = 1, .., n$ and $y(i)$ to the rows wih row indices $i = 1, .., m$.

5.1.1. Conversion from pixel to micrometer

The conversion factor from pixel to micrometer is estimated by measuring the inner diameter of the cuvette ($D = 9.66$ mm, $\sigma_D = 0.03$ mm, see section 3.1.1) in pixels on the radiographs.

On the radiographs the rim of the cuvette is darker than the fluidized bed because more x-ray is absorbed (cf. figure 12). This fact is used to identify the maximal change in the gray-scale value in x-direction with the left x_l and right x_r inner rim of the cuvette.

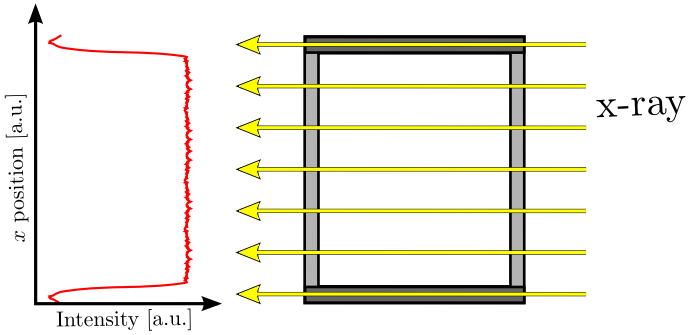

Figure 12: Identification of the maximal change in the intensity with the inner rim of the cuvette: Top view of the fluidization cell.

The gray-scale values of the radiographs are averaged row wise (see figure 13.1) and then the slope in x-direction is calculated numerically according to:

$$\mathrm{slope}(j) = \frac{\underset{i}{\mathrm{mean}}(j+2) - \underset{i}{\mathrm{mean}}(j)}{x(j+2) - x(j)} = \frac{\underset{i}{\mathrm{mean}}(j+2) - \underset{i}{\mathrm{mean}}(j)}{2},$$

where i indicates the row index and $x(j)$ the pixel-value of column j. Figure 13.2 shows the slope around the right rim.

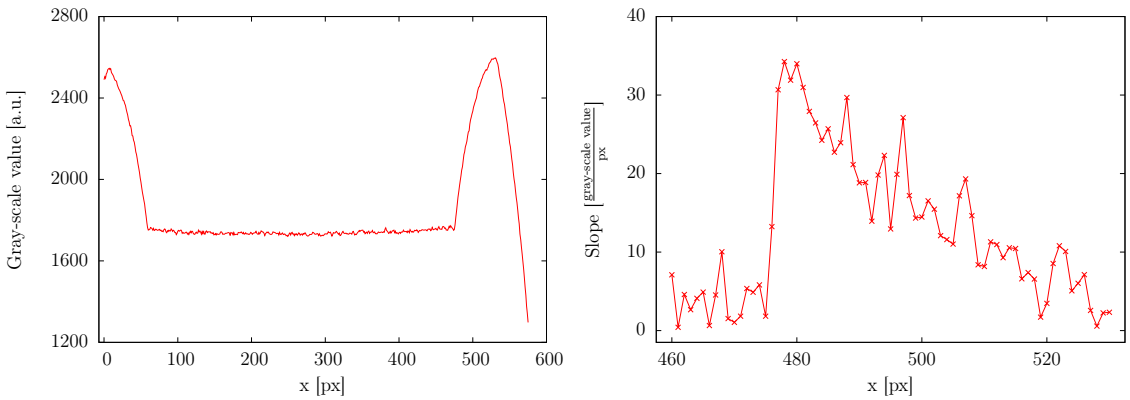

(13.1) Row wise averaged gray-scale value. **(13.2)** Calculated slope around the right rim.

Figure 13: Identification of the maximal change in the gray-scale value with the inner rim of the cuvette: Averaged gray-scale value and slope for an example radiograph.

The maximum slope is calculated for an area around the left and the right inner rim. For each run k the positions of the rim x_{l_k} and x_{r_k} are averaged over all radiographs, with sample standard deviation σ_{l_k} and σ_{r_k}. The inner diameter of the cuvette is

calculated for each run: $d_k = x_{\mathrm{r},k} - x_{\mathrm{l},k}$, the error is calculated using propagation of uncertainty $\sigma_{d_k} = \sqrt{\sigma_{\mathrm{l}_k}^2 + \sigma_{\mathrm{r}_k}^2}$.
Eventually the diameter d is averaged over all 19 runs at sample position $Z = +73$, the error calculates to $\sigma_d = \frac{1}{19}\sqrt{\sum_k \sigma_k^2}$. The conversion factor c is calculated according to:

$$\begin{aligned} c &= \frac{D}{d} &&= 22.52\ \tfrac{\mu\mathrm{m}}{\mathrm{px}} \\ \sigma_c &= \sqrt{\left(\tfrac{\sigma_D}{d}\right)^2 + \left(\tfrac{D\cdot\sigma_d}{d^2}\right)^2} &&= 0.06\ \tfrac{\mu\mathrm{m}}{\mathrm{px}}. \end{aligned}$$

5.1.2. Locating particles on radiographs

To locate tracer particles on radiographs a `MATLAB` routine was written. The program loops through all radiographs of one run given some parameters (*ROI, grayfilter, filter, area size, minimal* and *maximal amount of particles*) which are introduced below. The routine is introduced discussing an example workflow for one radiograph. Figure 14 depicts this workflow, the corresponding example radiograph is shown in figure 14.1. To illustrate the necessity of each step a worst case representative of the radiographs is used.
The radiograph is loaded as an array into `MATLAB`. In the first step the image is cut into the region of interest (*ROI*) (see figure 14.2 and 14.3), so particles are only located within the fluidized bed. The ROI needs to be determined by hand before starting the routine, but does not change through a whole run, as the fluidization cell does not move. In the example radiograph the ROI is very small due to the bad quality of the radiograph at the sides of the fluidized bed. This bad quality could lead to artifacts and should therefore be excluded from the analysis.
In the second step the mean gray-scale values are calculated row and column wise in the ROI (see figure 14.4). To account for density differences due to the bed construction – and in the example radiograph bad sensor calibration – every entry of the array is first cast from integer to double and then multiplied with the inverse mean gray-scale value of its row and column (the resulting picture is shown in figure 14.5):

$$\mathrm{pic}_{ij} = \frac{\mathrm{pic}_{ij}}{\underset{j}{\mathrm{mean}}(\mathrm{pic}_{ij}) \cdot \underset{i}{\mathrm{mean}}(\mathrm{pic}_{ij})}.$$

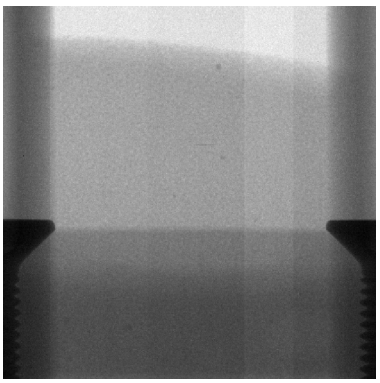

(14.1) Original radiograph taken by the `nanotom`.

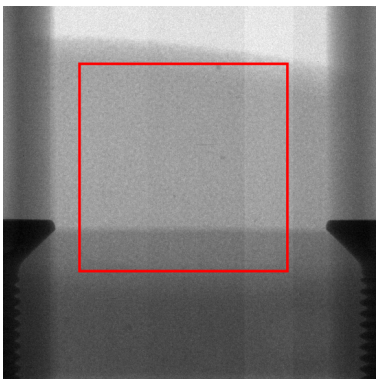

(14.2) Relevant and analyzable image section.

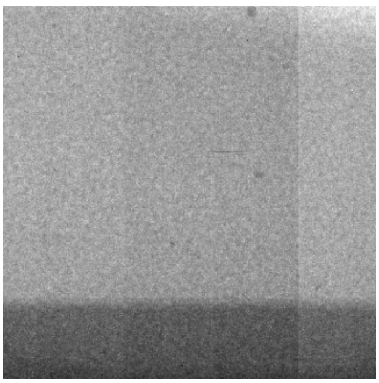

(14.3) Picture cut to the relevant image section (ROI).

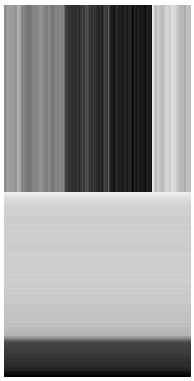

(14.4) Horizontal and vertical mean gray-scale values of the relevant image section.

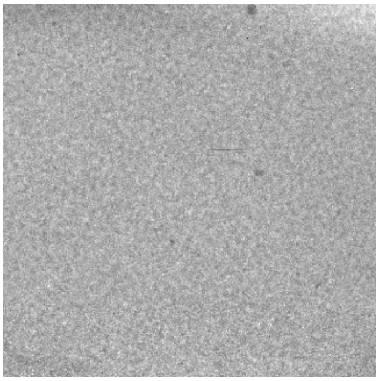

(14.5) Relevant image section modified with the mean gray-scale values.

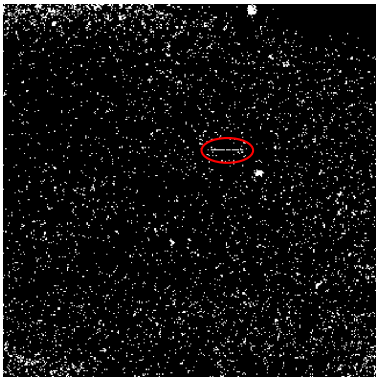

(14.6) Binary picture of the relevant image section, artifact labeled red.

(14.7) Filtered binary picture of the relevant image section.

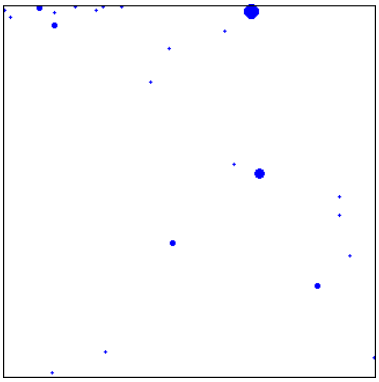

(14.8) Logical picture of size and centroids of white areas.

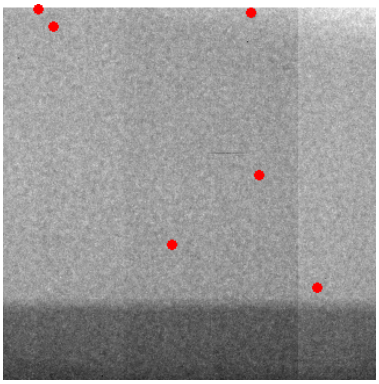

(14.9) Particles located in the relevant image section.

Figure 14: Image processing: Workflow of the routine, that locates particles on a radiograph.

In the third step a binary picture is created due to a binarization threshold (*grayfilter*), where the darkest pixels are labeled white (1) and all others black (0) (see figure 14.6). The gray-scale values of the radiographs fluctuate in a run (roughly about 5 %) due to the not constant beam and the air noise. To account for this fluctuation the grayfilter is varied by the program until a sufficient amount of particles is located (given a *minimal* and *maximal amount of particles* to locate). For faster computation the grayfilter should be roughly determined before starting the routine.
In the fourth step the picture is filtered to account for artifacts in the radiograph using the imerode function of `MATLAB` which applies a binary erosion. As a side effect all white areas shrink (see figure 14.7) and therefore particles can get lost. Thus this step should only be applied if there are artifacts in the picture, which should be checked before starting the routine (*filter*). An example artifact is marked red in figure 14.6.
In the last step a logical array is created from the filtered-picture. All white areas found are labeled by their area size and centroid (see figure 14.8). Particles with an insufficient area size are discarded. A sufficient *area size* has to be determined beforehand; mainly the tracer particles (see figure 14.9) should be left.
In the end the particle positions and the current picture ID are written to a file and the next radiograph is analyzed until the run is complete.

5.2. Particle tracking

This section describes the `MATLAB` routine implemented to track the particles located with the algorithm described in the previous section 5.1.2. The `MATLAB` routine loads all N particles of a run as an array with entries (x-position, y-position, time t_n), where $n = 0, 1, 2, ..., N$ and the time is indicated by the picture ID (1 pic $\hat{=}$ 1 timestep $\hat{=}$ 125 ms, cf. section 3.1.2).

Unambiguous assignment: A workflow of the particle tracking is shown in figure 15. The program starts the particle tracking with the first particle in the array $r_1(t_n)$ at the time $t_n = t_0$ (particle indicated red in figure 15.1). Then the distances $l_{ni} = l_{0i}$ to all possible next positions $r_i(t_{n+1}) = (x_i(t_{n+1}), y_i(t_{n+1})) = r_i(t_1)$ are calculated (all positions on the next picture $t_{n+1} = t_1$). The next picture is indicated

by the color gray in figure 15.1. The distances calculate to

$$l_{ni} = \sqrt{[x_i(t_{n+1}) - x_i(t_n)]^2 + [y_i(t_{n+1}) - y_i(t_n)]^2},$$

where $i = 1, 2, ...$ indicates the amount of particles located on the picture. The position $r_{\min}(t_{n+1}) = r_{\min}(t_1)$ with minimal distance $l_{n,\min} = l_{0,\min}$ is chosen to be the next position $r_1(t_1)$ of the particle (see figure 15.2). The previous particle position is deleted from the array (see figure 15.3), so it cannot be assigned to another particle track.

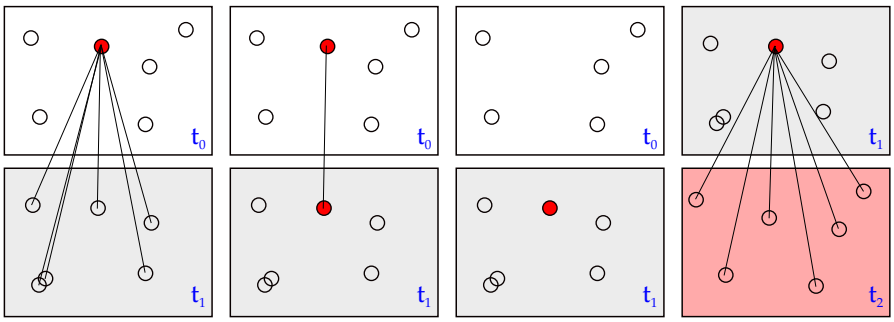

(15.1) **(15.2)** **(15.3)** **(15.4)**

Figure 15: Routine to find the next particle position, unambiguous assignment.

Now the routine starts calculating the distances $l_{(n+1)i} = l_{1i}$ between the new particle position $r_1(t_1)$ and the next possible positions $r_i(t_2)$ (see figure 15.4).
The routine loops through all timesteps until the particle is lost (see below). The particle track is written to a file and the program starts tracking the next particle in the array: $r_2(t_n)$.

Particle is declared lost: In case a previously detected particle cannot be located for a timestep the particle is declared lost. This happens, if the last picture of the run is reached or the next position was not detected (for example particle $r_2(t_0)$ indicated red in figure 16.1).
In the routine the next position cannot be assigned, if the distance to all possible next positions is larger than a maximal distance $l_{n,\max}$ (criterion given by the user). In this thesis *the maximal distance a particle can travel in one*

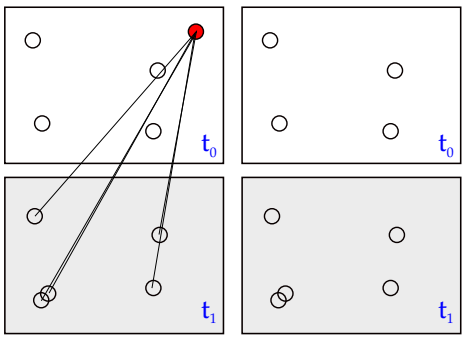

(16.1) **(16.2)**

Figure 16: Routine to find the next particle position, particle is declared lost.

timestep is used as a criterion. The values for different fluidization velocities are determined roughly from analyzing some radiographs. The position $r_2(t_0)$ – before the particle is lost – is deleted from the array (see figure 16.2) and the routine writes the track to a file. Then the next particle in the array $r_3(t_0)$ is tracked.

Figure 17: One particle detected two times.

Ambiguous assignment: A particle can be detected two times, if it is divided into two areas during binarization (see figure 17). This or two crossing particle trajectories leads to an ambiguous particle assignment, because the positions cannot be distinguished (e.g. particle $r_3(t_0)$, indicated red in figure 18.1). To account for this problem an averaged position is calculated if two particles are closer than a given distance (see figure 18.2). In this thesis *the particle radius* is used as a threshold. In case one of the ambiguous positions belongs to another trajectory the ambiguous positions are not deleted but labeled (see figure 18.5).

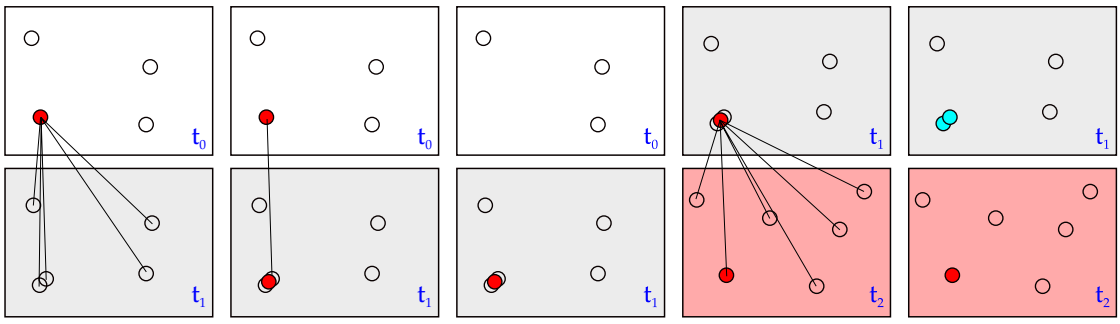

(18.1) **(18.2)** **(18.3)** **(18.4)** **(18.5)**

Figure 18: Routine to find the next particle position, ambiguous assignment.

The program tracks all particles until the last particle position in the array $r(t_N)$ is reached. Every particle track is stored in its own file. Given a limit for the track length, the routine automatically ignores tracks shorter than this threshold.

5.3. Resolution of the nanotom for a fixed bed

In this section the fluctuation of the particle position over time is calculated for the fixed beds of setup 3 - 5 to determine the noise level/resolution of the `nanotom`. The

position fluctuations occur due to the gray-scale value fluctuations on the radiographs (5 % for a run, 25 % between the setups). The gray-scale value fluctuations are caused by beam fluctuations, air noise and the change of the grayfilter, when locating the particles with the `MATLAB` routine.

A frequency count of the particle's x- and y-position over time was done for all particles tracked. The resulting histograms for two example particles taken from setup 5 are shown in figure 19.

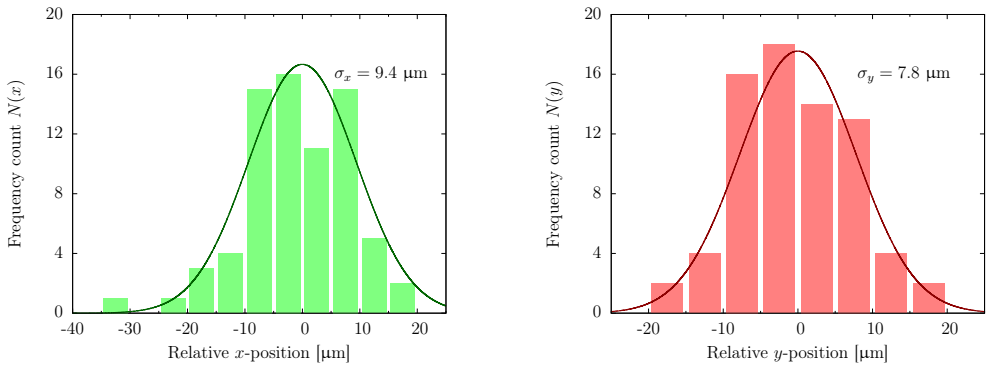

(19.1) Particle position relative to μ and GAUSS-fit (particle tracked for 73 timesteps $\hat{=}$ 9 s).

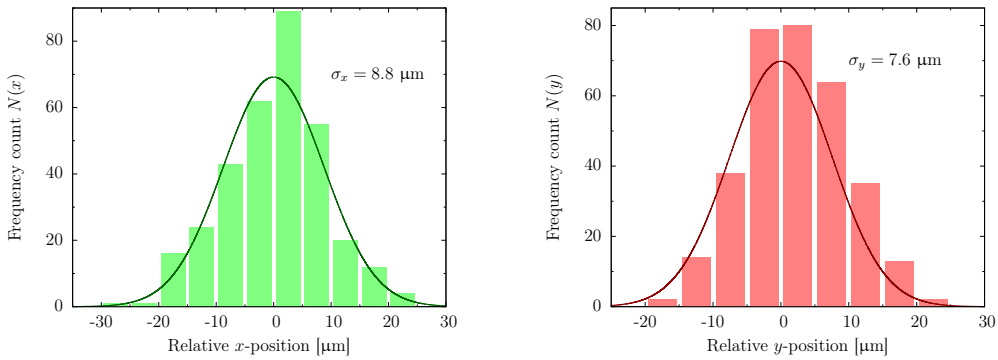

(19.2) Particle position relative to μ and GAUSS-fit (particle tracked for 327 timesteps $\hat{=}$ 41 s).

Figure 19: Determination of the position noise level: Example frequency counts ($\Delta = 5$ µm) and GAUSS-fits of the x- and y-position of two particles of different track length.

The frequency counts of the particle positions are GAUSSian distributed for track lengths > 70 steps $\hat{=}$ 8.75 s. All 15 particle tracks > 70 steps from setup 3 - 5 have been fitted using the normfit-function of `MATLAB`, which uses the function

$$g(x|\mu,\sigma) = \frac{1}{\sigma\sqrt{2\pi}} e^{-\frac{(x-\mu)^2}{2\sigma^2}}$$

and gives the mean value μ and standard deviation σ with error (95 % confidence interval) of the particle positions. Figure 19.1 and 19.2 show two example fits of the x- and y-position relative to μ of two particles of different track length.
Figure 20 shows a scatter plot of σ_x and σ_y for all 15 analyzed particles. The values are distributed in clusters on one line and are slightly shifting to the right. Therefore a systematic error must be involved.

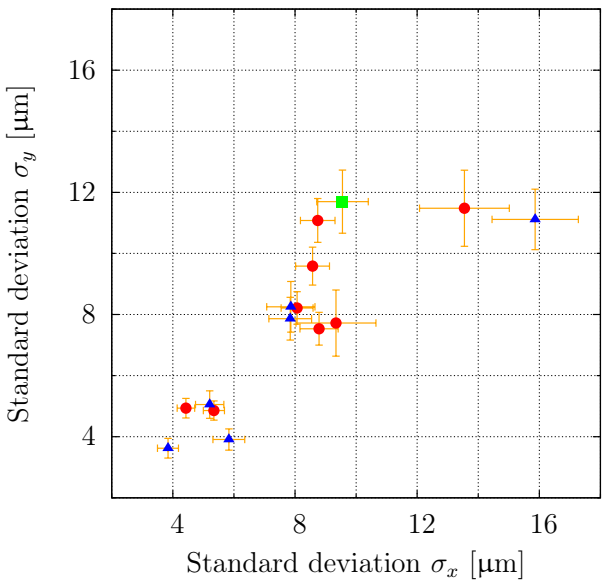

Figure 20: Determination of the position noise level: Scatter plot of the standard deviation σ_x and σ_y of 15 particles from setup 3 - 5. Setup 3 is indicated by green squares, setup 4 is indicated by blue triangles, setup 5 is indicated by red circles.

The 3 clusters do not correlate with the 3 setups, neither do they correlate with the track length. But they do correlate with the appearance of the particles on the radiographs. Very blurred and pale particles have a larger standard deviation than dark and very clear particles (see figure 21). Therefore one systematic error is the coating of the particles.

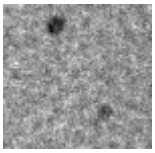

Figure 21: Systematic error: Particles with different coating thickness show a different resolution, due to the different x-ray absorption in the `nanotom`. The left particle exhibits a higher resolution (smaller deviation in the position noise level) than the right one.

The amount of 15 particles is not large enough to give an explicit value of the resolution. A noise-level of 20 µm in x- and y-direction is chosen to account for this inconvenience and the fact that the resolution of the `nanotom` will be different for moving particles and the broad interval length of $\Delta = 5$ µm. This noise level lies above the measuered standard deviations.

5.4. Reconstructed particle trajectories

This section discusses the particle trajectories computed from the different runs of setup 3 - 5. In general locating and tracking particles is satisfactory for fluidization velocities $3\ \frac{\text{ml}}{\text{min}} \leq v \leq 6\ \frac{\text{ml}}{\text{min}}$, for higher velocities the particles were too blurred to achieve good results.

For all runs convection cells are observed, their pattern depends on the height of the suspension (therefore depending on the amount of glass beads forming the bed and the flow rate), figure 22.2 shows a schematic illustration. As mentioned before leveling the cell results in a shift of the cell. The observed cell can be easily identified from the particle tracks (some example trajectories are plotted in figure 22.1). The graph depicts a part of the right side of the fluidization cell, indicated by a red square in figure 22.2. Due to the convection cells the planned analysis of particle diffusity seems to be impossible, as the particles move due to this overlaying movement.

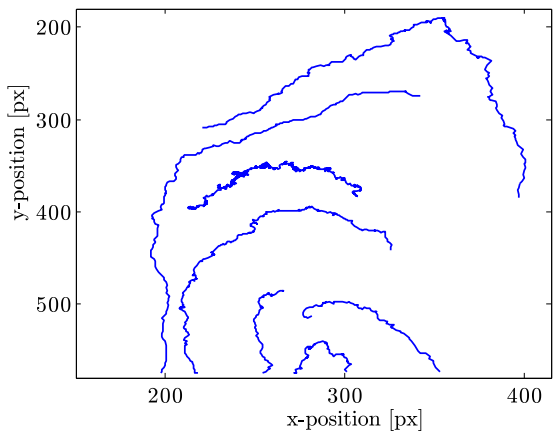

(22.1) Particle tracks in the area indicated by the red square in figure 22.2 (7 particles of setup 4 at $v = 4\ \frac{\text{ml}}{\text{min}}$).

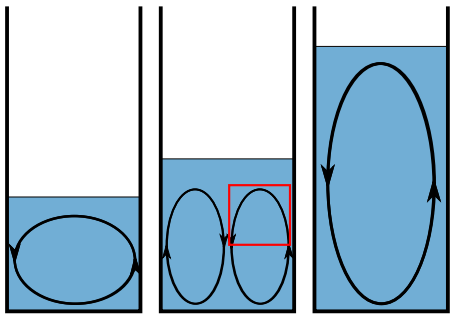

(22.2) Schematic illustration of different observed convection cells.

Figure 22: Observed convection cell.

5.5. Particle velocity

In this section the particle velocities of the particles tracked in setup 3 - 5 are analyzed in short segments. First the segmentation length that was used is discussed

and applied to the trajectories. Afterwards the segments are divided in those mainly undergoing convection in x-direction and those mainly undergoing convection in y-direction.

5.5.1. Representative segmentation length

For further analysis the particle trajectories are cut into representative segments. It is difficult to find a segmentation length representing all particles in one run. This can be seen in figure 23, where the chosen segmentation length of 40 steps ($\hat{=}$ 5 s) is plotted (orange) on top of the particle trajectories (blue). In some parts the segments represent the trajectories nicely (indicated by the green dots), in some parts the segmentation length is too long (indicated by black dots) and for some too short (indicated by red dots). Overall no segmentation length matching all tracks could be found. The segmentation length of 40 steps was chosen for further analysis.

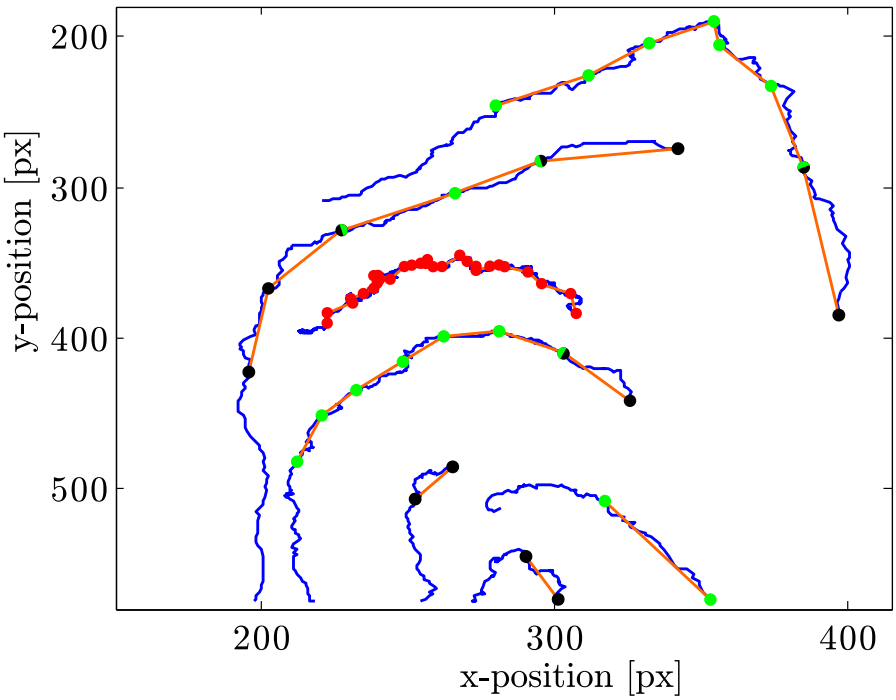

Figure 23: Applied segmentation length: Particle tracks (blue) of 7 particles of setup 4 at $v = 4\ \frac{\text{ml}}{\text{min}}$ and segments of 40 steps $\hat{=}$ 5 s (orange). Blue dots indicate the segments are representative, black dots they are too long and red dots they are too short.

5.5.2. Particle velocity in small segments

For fluidization velocities of $v = 3;\ 4;\ 5;\ 6\ \frac{\text{ml}}{\text{min}}$ the particle velocities in x- and y-direction for segments of 5 s

$$u_i = \frac{x_i(40) - x_i(1)}{5}\ \frac{\mu\text{m}}{\text{s}} \qquad \text{and} \qquad w_i = \frac{y_i(40) - y_i(1)}{5}\ \frac{\mu\text{m}}{\text{s}}$$

are plotted in figure 24. Negative velocities indicate particle movement from bottom to top, from left to right respectively. For random motion the particle velocities schould be GAUSSian-distributed around zero, the velocities in x- and y-direction roughly falling on the same graph. For the fluidized beds the velocities in y-direction show a peak at zero but have very long tails, whereas they are nearly GAUSSian-ditributed in x-direction.
Overall the particles travel faster in y-direction, which was expected because the observed convection cell was mainly dragging particles in that direction.

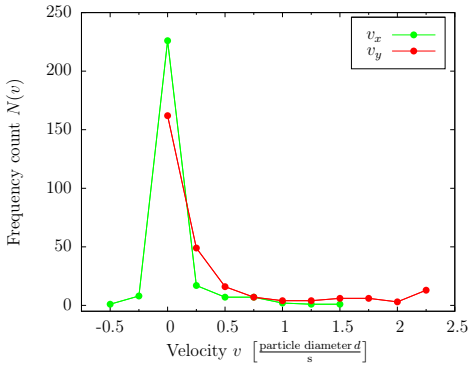

(24.1) 3 $\frac{\text{ml}}{\text{min}}$, 270 particles.

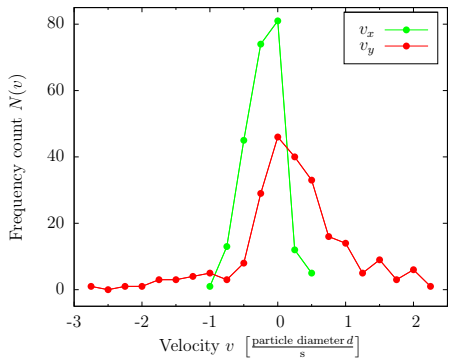

(24.2) 4 $\frac{\text{ml}}{\text{min}}$, 231 particles.

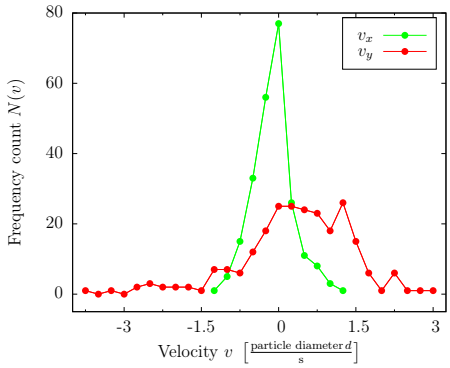

(24.3) 5 $\frac{\text{ml}}{\text{min}}$, 236 particles.

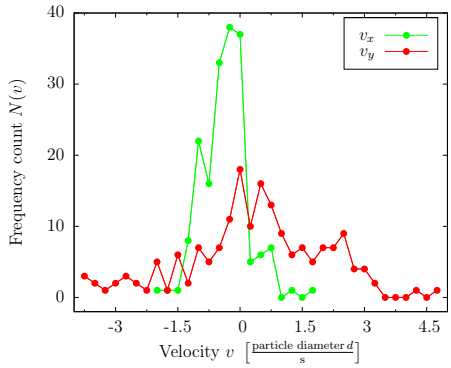

(24.4) 6 $\frac{\text{ml}}{\text{min}}$, 177 particles.

Figure 24: Particle velocities in the fluidized beds of setup 3 - 5. Analyzed in trajectory segments of 5 s. Particle diameter $d = 200\ \mu\text{m}$.

5.5.3. Criterion to divide segments

In general a fluidized bed not undergoing an overlaying macroscopic motion (like convection) is needed to study particle diffusity. With the given experimental setup no such measurement could be realized.
If every particle trajectory would be divided in parts mainly undergoing convection in x-direction and parts mainly undergoing convection in y-direction, diffusion-like behavior might be observed in the perpendicular direction. Therefore a general criterion to divide the introduced segments is needed.
In y-direction diffusion-like movement should occur if $v_y < v_x$, figure 25.1 shows some particle trajectories of setup 4 ($v = 4\ \frac{\text{ml}}{\text{min}}$) where the parts fulfilling this criterion are indicated orange.
In x-direction the criterion $v_x < v_y$ is not strong enough, because the particles are traveling faster in y-direction. Therefore the criterion is tightened to $v_x < \frac{v_y}{2}$ (cf. figure 25.2).

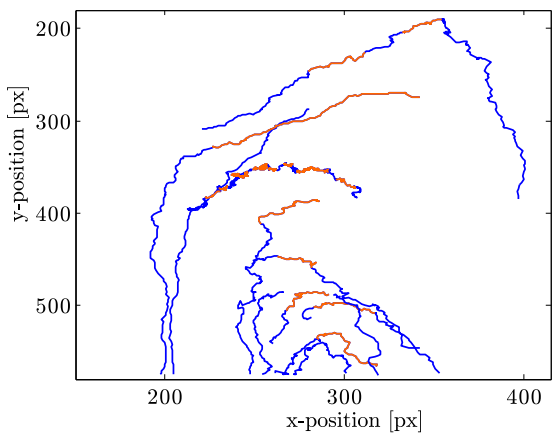

(25.1) Criterion for diffusion-like movement in y-direction, the orange part of the trajectory fulfills the criterion $v_y < v_x$.

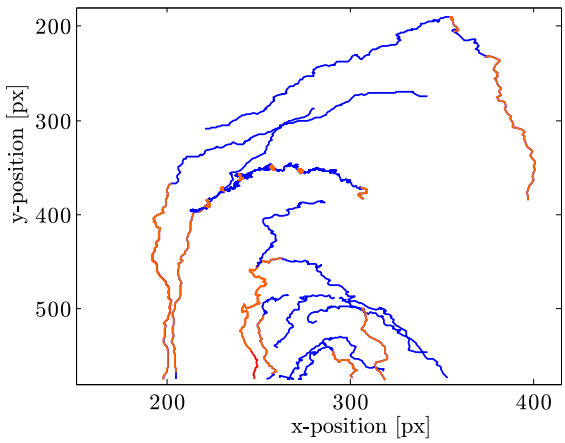

(25.2) Criterion for diffusion-like movement in x-direction, the orange parts fulfill the criterion $v_x < \frac{v_y}{2}$.

Figure 25: Example particle trajectories (indicated blue) of setup 4 for $v = 4\ \frac{\text{ml}}{\text{min}}$.

Figure 25 shows that the proposed criteria seem reasonable. In figure 26 the particle velocities in x- and y-direction and the particle velocities when applying the criterion for diffusion-like movement are plotted. The velocities seem to be GAUSSian distributed, when applying the criterion.

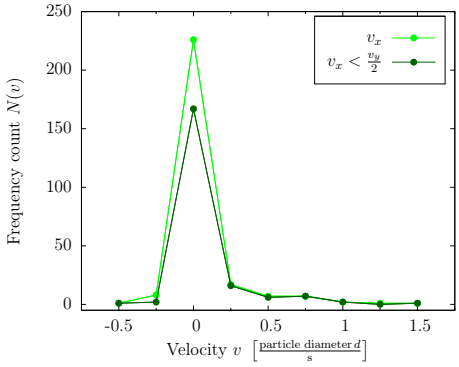

(26.1) 3 $\frac{\text{ml}}{\text{min}}$, $N = 270$, $N_c = 202$.

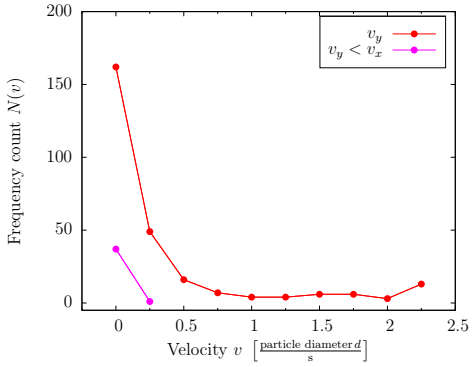

(26.2) 3 $\frac{\text{ml}}{\text{min}}$, $N = 270$, $N_c = 38$.

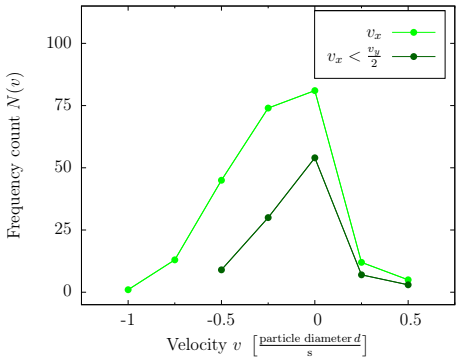

(26.3) 4 $\frac{\text{ml}}{\text{min}}$, $N = 231$, $N_c = 103$.

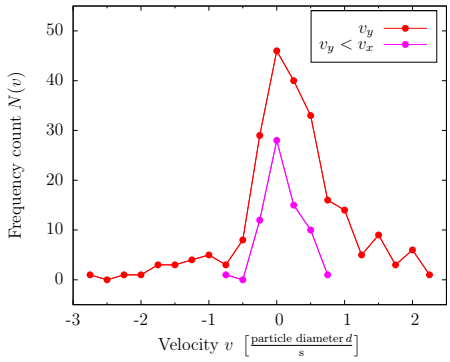

(26.4) 4 $\frac{\text{ml}}{\text{min}}$, $N = 231$, $N_c = 67$.

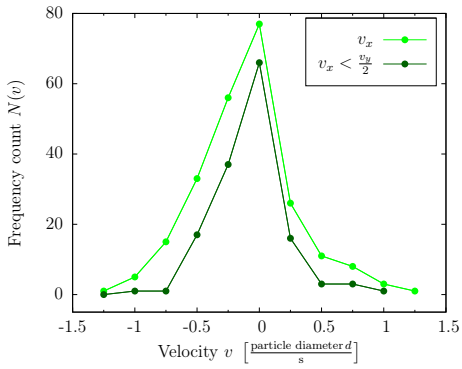

(26.5) 5 $\frac{\text{ml}}{\text{min}}$, $N = 236$, $N_c = 145$.

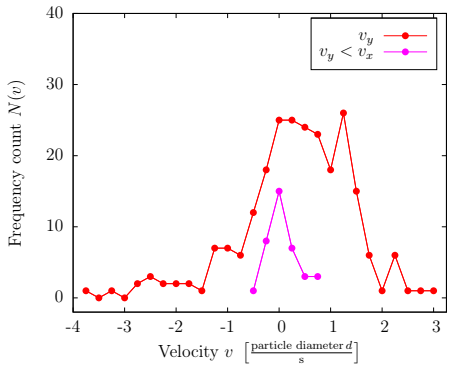

(26.6) 5 $\frac{\text{ml}}{\text{min}}$, $N = 236$, $N_c = 37$.

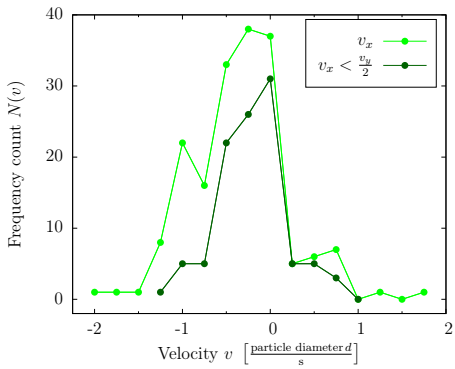

(26.7) 6 $\frac{\text{ml}}{\text{min}}$, $N = 177$, $N_c = 103$.

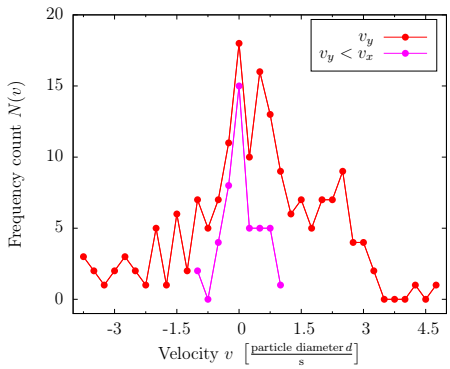

(26.8) 6 $\frac{\text{ml}}{\text{min}}$, $N = 177$, $N_c = 45$.

Figure 26: Comparison of the particle velocities to those when applying the criterion for diffusion-like movement, N gives the amount of particles analyzed, N_c the amount of particles fulfilling the criterion. Particle diameter $d = 200$ µm.

5.6. Mean squared displacement

In this section the mean squared displacement (MSD) of the particle trajectories from setup 3 - 5 is analyzed. In the first part a *pseudo*-ensemble MSD is calculated for sets of particles cut to the segmentation length discussed in the previous chapter, in the second part the time-averaged MSD for one single particle trajectory is analyzed.

The MSD is calculated with a `MATLAB` routine using equations (2) and (3) given in section 2.1.3. The resulting data are fitted with `Gnuplot` [23] which uses the MARQUARDT-LEVENBERG-algorithm. The errors calculated by the algorithm are not listed in this thesis as they are smaller than the real ones.
Before applying the routine on the fluidized beds it is applied to two random walks of 40 000 steps, which are numerically simulated with `MATLAB`. Figure 27 shows the first 200 steps of these simulated walks.

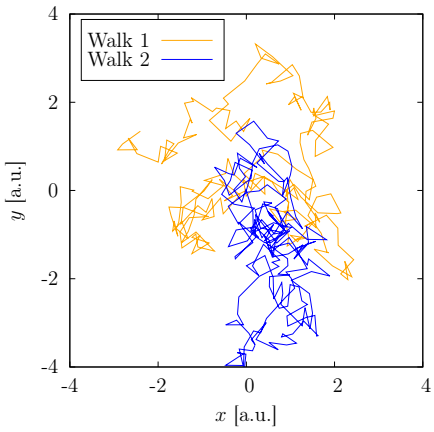

Figure 27: First 200 steps of two random walks of 40 000 steps simulated with `MATLAB`.

In general the MSD follows an exponential law ($\text{MSD} = k \cdot \tau^m$). Diffusive behavior is identified by the exponent $m = 1$ (see equation 1). Therefore the MSD calculated with `MATLAB` is plotted on a log-log scale and fitted via linear regression:

$$\log(\text{MSD}) = m \cdot \log(\tau) + \log(k) \Rightarrow f(t) = m \cdot t + b, \tag{4}$$

where $\log \text{MSD} = f(t)$, $\log(\tau) = t$, $\log(k) = b$. The parameter k is proportional to the diffusion coefficient. Due to the observed convection cell the diffusion coefficient cannot be determined and only the exponent m (slope of the linear fit) is analyzed. Therefore the offset b is not listed.

5.6.1. Mean squared displacement of a set of particles

In all three setups few particles could be tracked and many only for a short time. For this reason no real ensemble MSD can be calculated. Therefore the trajectories are cut into small segments of 40 steps (as discussed above), where every segment is han-

dled as a trajectory. Calculating a *pseudo*-ensemble MSD for these segments works for a diffusive system, where the time-averaged and ensemble MSD are consistent. In the three setups convection is observed, therefore this segmentation should not be allowed. When the segments are divided in parts mainly undergoing convection in x- or y-direction calculating the *pseudo*-ensemble MSD might work.

Random walk

First the *pseudo*-ensemble MSD in x- and y-direction is calculated for the random walks (cf. figure 27) to test the procedure. Each walk is cut into 975 segments of 40 steps. The curves are fitted via equation (4) and plotted on a log-log scale in figure 28.

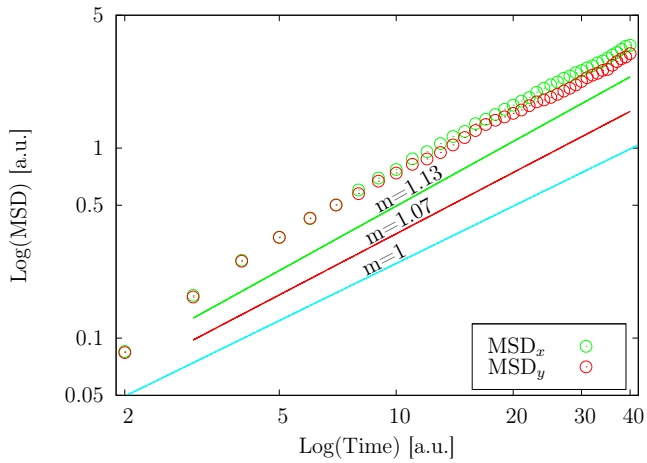

Figure 28: *Pseudo*-ensemble MSD of two random walks (cf. figure 30). The walks are cut into segments of 40 steps (resulting in 1950 segments). The fitted curves are plotted with a different offset.

Except for the second timestep (corresponds to the first timestep in the plot, as the real first timestep MSD = 0 is not plotted) the MSDs in x- and y-direction fall nicely on one line, for the first 10 timesteps even on the same line. After 10 timesteps the MSDs in x- and y-direction slightly diverge.

The discrepancy in the second step may be explained by the fact, that only few steps of the whole random walk are taken into account. For the first timestep 1950 steps of the random walk are analyzed, whereas for the second $2 \cdot 1950$ and for the third $3 \cdot 1950$ are analyzed. Therefore the discrepancy could be explained by the small amount of steps.

Due to this discrepancy the linear regression is only applied for timesteps > 2, resulting in:

$$\mathrm{MSD}_x(\tau) \propto \tau^{1.13} \text{ and } \mathrm{MSD}_y(\tau) \propto \tau^{1.07}.$$

This is roughly a slope of $m = 1$ for both the MSD in x- and y-direction and therefore the random walks show diffusive behavior when analyzing the *pseudo*-ensemble MSD without the first and second timestep. The slight deviation from $m = 1$ most probably is due to the bad quality of the rand-function of MATLAB, which seems to not really create random numbers.

Particle trajectories

The particle trajectories from the three setups are cut into segments of 40 steps and divided in those undergoing mainly convection in x-direction and those mainly undergoing convection in y-direction (cf. section 5.5.3). The *pseudo*-ensemble MSD is calculated in x- and y-direction for these parts (cf. figure 29).
In x-direction a linear regression is applied to all but the first two timesteps and the timesteps undercutting the noise level. In y-direction very few particles remain after applying the criterion (cf. figure 26), the MSD does not show a linear behavior over long intervals and only few data points are included in the fit.

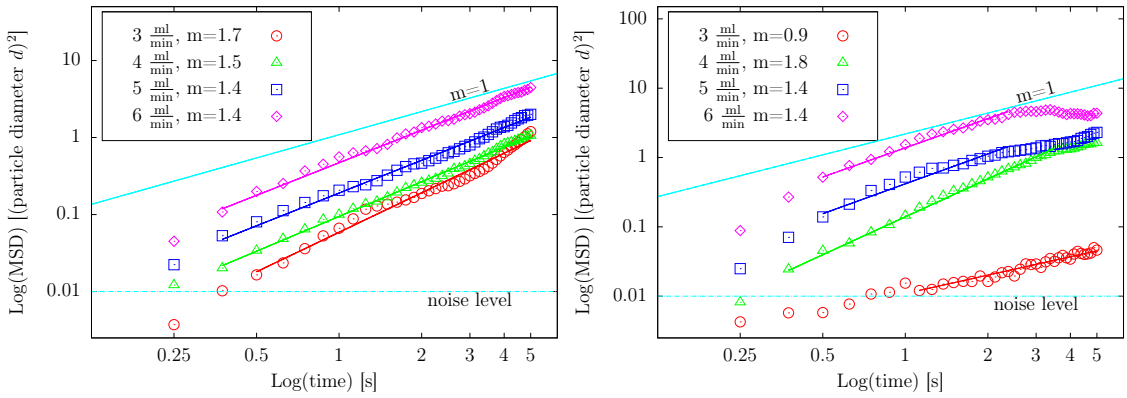

(29.1) MSD in x-direction for particle trajectories $v_x < \frac{v_y}{2}$.

(29.2) MSD in y-direction for particle trajectories $v_y < v_x$.

Figure 29: *Pseudo*-ensemble MSD of setup 3 - 5: analyzed in segments of 40 steps. In y-direction only few particles are analyzed: For all but $v = 4\ \frac{\text{ml}}{\text{min}}$ only $20 - 50$ segments could be analyzed. Noise-level: 20 µm; particle diameter $d = 200$ µm.

Figure 29 shows that the MSD increases when increasing the fluidization velocity, which means that the particle movement increases.
The slope of the MSD in x-direction roughly gives a value of $m_x = 1.5\ \frac{\mu\text{m}^2}{\text{s}}$. No diffusion-like behavior ($m = 1$) is observed. This means that the criterion is not

chosen wisely or the particles do not show diffusion-like behavior in x-direction when mainly undergoing convection in y-direction. A stronger criterion would result in too few particles to analyze, therefore the approach should be dismissed.
In y-direction no overall slope can be found. Only few particles remain for the given criterion, the MSDs do not fall on a straight line. The approach should be dismissed for the MSD in y-direction as well.
No overall criterion for diffusion-like behavior could be found with the given experimental setup.

5.6.2. Mean squared displacement of one trajectory

As the approach tried above does not work the time-averaged MSD of one single particle trajectory is calculated to see, if diffusion-like behavior can be found.

Random walk

First the time-averaged MSD for a random walk (indicated green in figure 27) is analyzed to test the procedure. The time-averaged MSD is plotted on a log-log scale in figure 30.

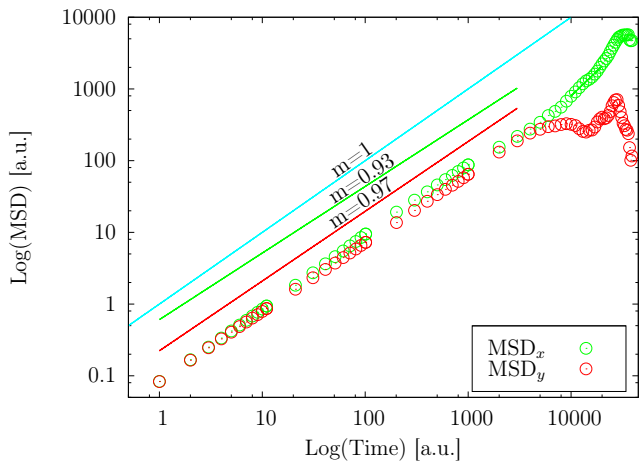

Figure 30: Time-averaged MSD of a random walk (indicated green in figure 27). Only data points for multiples of 10 (including 10^0) are plotted. A fit of the first 3000 steps is performed.

For the first 10 steps the data of MSD$_x$ and MSD$_y$ fall nicely on one line. After that they slightly diverge up to a value of roughly 3000 steps. For more than 3000 steps the MSD in y-direction stagnates, while the MSD in x-direction keeps increasing.
The divergence for long time intervals can again be explained by the bad quality

of the rand-function of `MATLAB`. Another reason could be that the long intervals do not represent the movement sufficiently and the amount of intervals decreases. Due to this divergence the linear regression is only applied to the first 3000 steps of the random walk:

$$\mathrm{MSD}_x(\tau) \propto \tau^{0.93} \text{ and } \mathrm{MSD}_y(\tau) \propto \tau^{0.97}.$$

This is roughly a slope of $m = 1$ for both the MSD in x- and y-direction and therefore the random walk shows diffusion-like behavior when analyzing the time-averaged MSD for a thirteenth of the whole track. Analysis for the whole track results in a slightly higher slope in x-direction and a slightly lower slope in y-direction.

Particle trajectory

The time-averaged MSD is calculated for one particle trajectory. Figure 31.1 shows the analyzed trajectory (1296 steps $\hat{=}$ 162 s), which is chosen because it shows a very slow particle velocity and therefore hopefully only undergoes minor convection. The MSD is calculated for the part of the trajectory undergoing mainly convection in x-direction (598 steps $\hat{=}$ 74.75 s). The part is indicated orange in figure 31.1. The MSD is shown in figure 31.2. The MSDs do not fall on one straight line. They diverge from the beginning (only for $t < 0.5$ s they are similar).

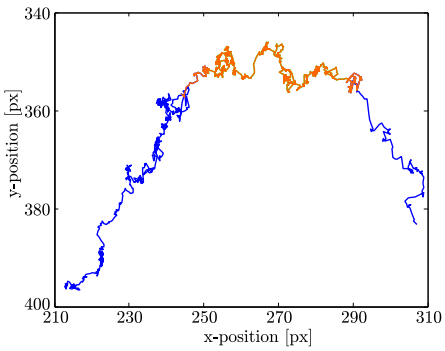

(31.1) Particle trajectory: Orange indicates the part where convection in x-direction and diffusion-like movement in y-direction is expected.

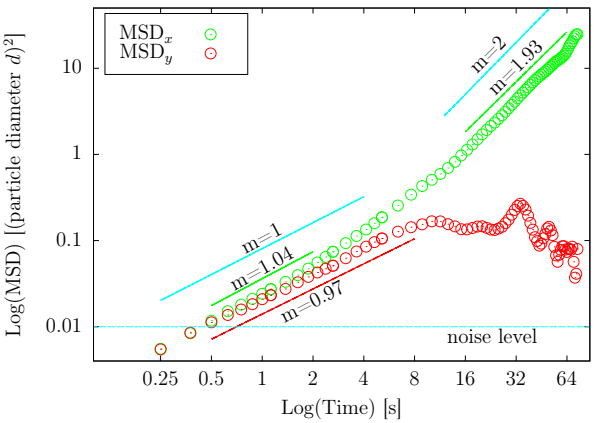

(31.2) Time-averaged MSD for the orange trajectory (not all data are plotted); length: 74.75 s; fit for MSD_x: [0.5 s, 2 s] and [16 s, 64 s]; fit for MSD_y: [0.5 s, 8 s]. Noise-limit: 20 µm; particle diameter $d = 200$ µm.

Figure 31: Analysis of a single particle trajectory of setup 4, $v = 4\ \frac{\mathrm{ml}}{\mathrm{min}}$.

It seems that the MSD in x-direction shows a change of slope, with a smooth and broad overlapping area. Therefore the MSD in x-direction is fitted in two intervals [0.5 s, 2 s] and [16 s , 64 s] using equation (4). The movement in x-direction shows diffusion-like behavior ($m = 1.04 \approx 1$) for short time intervals $\tau < 2$ s and convection $m = 1.93 \approx 2$ for large time intervals $\tau > 16$ s.
The MSD in y-direction stagnates for times > 8 s, the particle seems to be bound by the convection cell. Therefore MSD_y is fitted in the interval [0.5 s, 8 s]. The fit results in $m = 0.97$, diffusion-like behavior.

The observed diffusion-like behavior could be originating in rounding errors or the noise of the nanotom, because it is only observed for very small particle movements ($< \frac{d}{2}$). Therefore the procedure is applied to another trajectory (a particle moving faster than the previous one, see figure 32).

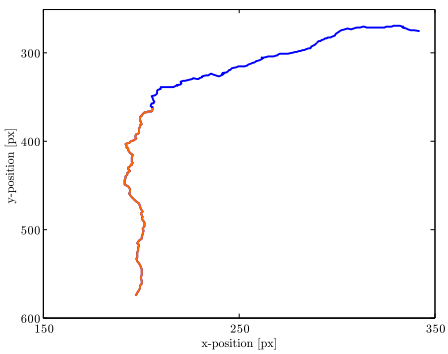

(32.1) Particle trajectory.

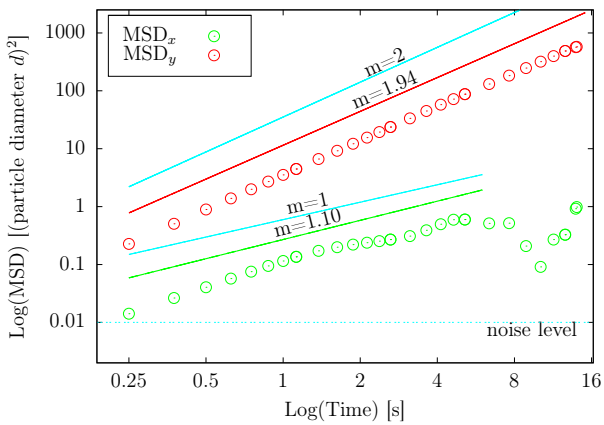

(32.2) Time-averaged MSD (not all data are plotted); fit for MSD_x: [0.25 s, 6 s], MSD_y: [0.25 s, 20 s].

Figure 32: Analysis of a single particle trajectory of setup 4, $v = 4\ \frac{\text{ml}}{\text{min}}$. Orange indicates the part (length: 20 s) for which the MSD is analyzed (convection in y-direction and diffusion-like movement in x-direction is expected). Noise-limit: 20 µm; particle diameter $d = 200$ µm.

The particle shows convective behavior in y-direction. In x-direction diffusion-like behavior is observed for small timescales, for longer timescales the movement stagnates (similar to the movement in y-direction of the previous particle). Again the diffusion-like behavior is only observed for short distances and could therefore be originating in rounding errors or noise. The reason for the observed diffusion-like behavior in x-direction of the first particle could lay in the very slow movement of this particle, as no similar movement is observed for the faster particle.

6. Conclusion

Due to the flawed experimental setup, this thesis could not provide a result on the larger topic of the glass transition phenomenon. The fluidization cell used is not suitable: An underlaying systematic experimental error (a shift in the cell construction) manifesting in a convection cell, made it impossible to analyze uninfluenced particle movements.

Dynamics

On the microscopic scale, it is shown that for a fluidized bed undergoing convection, the particle velocity increaes when increasing the flow rate. The particle diffusity could not be analyzed. Therefore, the inital idea behind this thesis – to determine flow-rate-dependent diffusion coefficients – could not be realized. Analyzing single particle trajectories it is shown, that the convective behavior can be confirmed while calculating the MSD. Diffusion-like movement occurs for small timescales perpendicular to the convection; whereas for longer timescales, the particles seem to be bound by the convection cell. For the macroscopic movement, no conclusions could be drawn.

Tracer particles

Still, this thesis provides insights in the behavior of different types of tracer particles used, which is of importance for subsequent work with the `nanotom`. Working with coated particles is not really satisfactory for particle tracking, because the density difference between the fluidized bed and the tracer particles is very small, resulting in nearly the same x-ray absorption.

The scope for improvement is given in figure 33: The figure shows a radiograph of borosilicate *MoSci* glass beads with naturally occuring impurities. Usually, these particles are seperated from the glass beads when working with fluidized beds, but they seem like quite promising tracer particles.

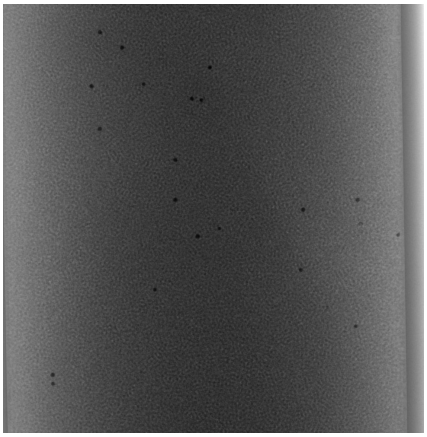

Figure 33: Possible tracer particles: Radiograph of borosilicate *MoSci* glass beads with naturally occuring impurities.

Future direction

However, a set of enhancements that should allow a conclusive measurement in the future can be proposed:
Overall a new fluidization cell should be built, with no shift and the possibility to level it very nicely inside the `nanotom`. To realize the analysis of macroscopic motion, a smaller cuvette should be used to account for the 3D effect which was mentioned in chapter 4. While using a different x-ray unit, it might be possible to take radiographs with a shorter exposure time, which should result in a better resolution of the density fluctuations.

A. Wet chemical coating of silver tracers

Protocol from Julie Murison:

50.0 $\frac{g}{L}$ $AgNO_3$ solution, with sufficient NH_4OH (25 %) added until all silver has formed the $Ag[NH_3]_2$ complex, as indicated by dissolution of all brown $AgNH_3$ precipiate resulting in a clear solution.
The reactive mixture is poured over glass grains. To this solution is added formaldehyde (2.5 ml per 10 ml H_2O). The solution is left to plate for 120 min at room temperature. The grains are rinsed with isopropanol.

B. Bibliography

[1] D. Goldman and H.L. Swinney. *Signatures of glass formation in a fluidized bed of hard spheres. Physical Review Letters*, **96**, 14: p. 145702, **2006**.

[2] G. E. Uhlenbeck and L. S. Ornstein. *On the Theory of the Brownian Motion. Physical Review*, **36**: pp. 823–841, **1930**.

[3] *Welt der Physik*, **20.1. 2013**. URL `http://www.weltderphysik.de/gebiete/atome/atome-und-quantenphysik/`.

[4] A. Einstein. *Über die von der molekularkinetischen Theorie der Wärme geforderte Bewegung von in ruhenden Flüssigkeiten suspendierten Teilchen. Annalen der Physik*, **322**, 8: pp. 549–560, **1905**.

[5] A. Lubelski *et al.* *Nonergodicity Mimics Inhomogeneity in Single Particle Tracking. Physical Review Letters*, **100**, 25: p. 250602, **2008**.

[6] I.F. Sbalzarini and P. Koumoutsakos. *Feature Point Tracking and Trajectory Analysis for Video Imaging in Cell Biology. Journal of Structural Biology*, **151**, 2: pp. 182 – 195, **2005**.

[7] R. Hovius *et al.* *Single Molecule Detection with Atto 647N NTA*, **2006**. URL `http://www.sigmaaldrich.com/technical-do\hskip\z@cuments/articles/biofiles/single-molecul\hskip\z@e-detection.html`.

[8] J. Duran. *Sands, powders, and grains: An Introduction to the Physics of Granular Materials.* Springer-Verlag, **2000**. ISBN 0-387-98656-1.

[9] J.F. Métayer *et al.* *Shearing of frictional sphere packings. Europhysics Letters*, **93**, 6: p. 64003, **2011**.

[10] G.R. Farrell, M. Martini and N. Menon. *Loose packings of frictional spheres. Soft Matter*, **6**, 13: pp. 2925–2930, **2010**.

[11] M. Jerkins *et al. Onset of Mechanical Stability in Random Packings of Frictional Spheres. Physical Review Letters*, **101**, 1: p. 018301, **2008**.

[12] A. Deboeuf *et al. Segregation and periodic mixing in a fluidized bidisperse suspension. New Journal of Physics*, **13**, 7: p. 075005, **2011**.

[13] W. Pätzold. *Dynamik Von Angetriebenen Suspensionen.* Master's thesis, Georg-August-University of Göttingen, **2012**. At the Max Planck Institute for Dynamics and Self-Organization, Department: Dynamics of Complex Fluids.

[14] J.F. Richardson and W.N. Zaki. *Sedimentation and Fluidisation: Part I. Trans. Inst. Chem. Eng.*, **32**: pp. 35–53, **1954**.

[15] M. Schröter, D. Goldman and H.L. Swinney. *Stationary state volume fluctuations in a granular medium. Physical Review*, **71**, 3: p. 030301(R), **2005**.

[16] S. Sundaresan. *Instabilities in fluidized beds. Annual Review of Fluid Mechanics*, **35**: pp. 63–88, **2003**.

[17] Y.D. Sobral and F.R. Cunha. *A linear stability analysis of a homogeneous fluidized bed. Ten. em Mat. Aplicada e Comp.*, **3**, 2: pp. 197–206, **2002**.

[18] D. Geldart. *Types of Gas Fluidisation. Powder Technology*, **7**, 5: p. 285–292, **1973**.

[19] G. Houghton. *Particle and Fluid Diffusion in Homogeneous Fluidization. Ind. Eng. Chem. Fundamen.*, **5**, 2: pp. 153–164, **1966**.

[20] P.K. Dixon and D.J Durian. *Speckle Visibility Spectroscopy and Variable Granular Fluidization. Physical Review Letters*, **90**, 18: p. 184302, **2003**.

[21] *phoenix-xray.com, ge-mcs.com*, **20.9. 2012**. URL `http://www.ge-mcs.com/de/radiography-x-ray/ct-computed-tomography/nanotom-s.html`.

[22] *Matlab*, **29.12. 2012**. URL `http://www.mathworks.com/`.

[23] *Gnuplot*, **29.12. 2012**. URL `http://www.gnuplot.info/`.

Acknowledgements

I would like to express my gratitude to all those who made it possible to write this thesis.

- Dr. Matthias Schröter for giving me the opportunity to write my bachelor thesis in the area of statistical mechanics of granular media and of course for being the first referee of my thesis. It has been very joyful to work in his research group and I especially want to thank him for giving me the opportunity to join a beam time at the ESRF in Grenoble.
- Prof. Dr. Sarah Köster for being the second referee of my thesis.
- Welm Pätzhold for introducing me to the experimental setup and proof-reading my thesis.
- Julie Murison, Anna Marie Pries, Udo Krafft, Ulrich Vetter and Hans-Gregor Gehrke for the help with the coating of the tracer particles.
- Wolf Keiderling and the workshop of fine mechanics for the help when designing the nanotom desk.
- All people who proof-read my thesis: Fabian Wilk, Wilfried Schumann, Felix Gadeberg, Junaid Laskar.

Erklärung nach §13(8) der Prüfungsordnung für den Bachelor-Studiengang Physik und den Master-Studiengang Physik an der Universität Göttingen:

Hiermit erkläre ich, dass ich diese Abschlussarbeit selbständig verfasst habe, keine anderen als die angegebenen Quellen und Hilfsmittel benutzt habe und alle Stellen, die wörtlich oder sinngemäß aus veröffentlichten Schriften entnommen wurden, als solche kenntlich gemacht habe.
Darüberhinaus erkläre ich, dass diese Abschlussarbeit nicht, auch nicht auszugsweise, im Rahmen einer nichtbestandenen Prüfung an dieser oder einer anderen Hochschule eingereicht wurde.

Göttingen, den 1. Februar 2013

(Sara Lea Gadeberg)